

Three-dimensional variational assimilation of MODIS aerosol optical depth: Implementation and application to a dust storm over East Asia

Zhiquan Liu,¹ Quanhua Liu,² Hui-Chuan Lin,¹ Craig S. Schwartz,¹ Yen-Huei Lee,¹ and Tijian Wang³

Received 26 April 2011; revised 3 October 2011; accepted 4 October 2011; published 9 December 2011.

[1] Assimilation of the Moderate Resolution Imaging Spectroradiometer (MODIS) total aerosol optical depth (AOD) retrieval products (at 550 nm wavelength) from both Terra and Aqua satellites have been developed within the National Centers for Environmental Prediction (NCEP) Gridpoint Statistical Interpolation (GSI) three-dimensional variational (3DVAR) data assimilation system. This newly developed algorithm allows, in a one-step procedure, the analysis of 3-D mass concentration of 14 aerosol variables from the Goddard Chemistry Aerosol Radiation and Transport (GOCART) module. The Community Radiative Transfer Model (CRTM) was extended to calculate AOD using GOCART aerosol variables as input. Both the AOD forward model and corresponding Jacobian model were developed within the CRTM and used in the 3DVAR minimization algorithm to compute the AOD cost function and its gradient with respect to 3-D aerosol mass concentration. The impact of MODIS AOD data assimilation was demonstrated by application to a dust storm from 17 to 24 March 2010 over East Asia. The aerosol analyses initialized Weather Research and Forecasting/Chemistry (WRF/Chem) model forecasts. Results indicate that assimilating MODIS AOD substantially improves aerosol analyses and subsequent forecasts when compared to MODIS AOD, independent AOD observations from the Aerosol Robotic Network (AERONET) and Cloud-Aerosol Lidar with Orthogonal Polarization (CALIOP) instrument, and surface PM₁₀ (particulate matter with diameters less than 10 μm) observations. The newly developed AOD data assimilation system can serve as a tool to improve simulations of dust storms and general air quality analyses and forecasts.

Citation: Liu, Z., Q. Liu, H.-C. Lin, C. S. Schwartz, Y.-H. Lee, and T. Wang (2011), Three-dimensional variational assimilation of MODIS aerosol optical depth: Implementation and application to a dust storm over East Asia, *J. Geophys. Res.*, 116, D23206, doi:10.1029/2011JD016159.

1. Introduction

[2] Monitoring the distribution of atmospheric aerosols is crucial to understanding how aerosols impact regional air quality and human health [Pope *et al.*, 2002]. Moreover, it has been shown that a correct description of aerosols can improve global weather forecasts by reducing errors in precipitation and wind [Rodwell, 2005]. Aerosols have also been under the spotlight of climate research for a number of years because of their direct and indirect impact on radiative balance and interaction with other radiatively/dynamically active components of the earth system, such as clouds [Forster *et al.*, 2007].

[3] Yet, uncertainty still remains on the net radiative effect of aerosols, and research is ongoing to quantify aerosol properties and impact on weather and climate using both observational and numerical approaches. Regarding observational methods, ground-based observing networks such as the Aerosol Robotic Network (AERONET) [Holben *et al.*, 1998], European Aerosol Research Lidar Network (EARLINET) [Amiridis *et al.*, 2005], and Micro-Pulse Lidar Network (MPLNET) [Welton and Campbell, 2002], have been important in improving understanding of aerosols within the entire earth system. However, ground-based platforms only cover relatively small spatial areas. Observations from satellite platforms [Kaufman *et al.*, 2002] offer a more global view of aerosol distribution. Since 1988, the National Oceanic and Atmospheric Administration (NOAA) has provided operational aerosol optical depth (AOD) retrieval products from the Advanced Very High Resolution Radiometer (AVHRR) on board NOAA satellites [Ignatov *et al.*, 2004]. Furthermore, a number of other space-borne

¹National Center for Atmospheric Research, Boulder, Colorado, USA.

²Joint Center for Satellite Data Assimilation, Camp Springs, Maryland, USA.

³School of Atmospheric Science, Nanjing University, Nanjing, China.

instruments, such as the Moderate Resolution Imaging Spectroradiometer (MODIS) [Remer *et al.*, 2005], Multiangle Imaging Spectroradiometer (MISR) [Kahn *et al.*, 2010], Total Ozone Mapping Spectrometer (TOMS) [Torres *et al.*, 2002], and Ozone Monitoring Instrument (OMI) [Torres *et al.*, 2007] provide multispectral and multiangle aerosol measurements. An overview of various aerosol retrieval techniques is given by King *et al.* [1999].

[4] Efforts have also focused on numerical modeling and prediction of aerosols, which is usually associated with a large degree of uncertainty related to aerosol emission, transport, and interaction with nonlinear physical processes (e.g., radiative effects, cloud and precipitation formation). Data assimilation (DA), a statistically optimal approach combining observations and numerical model output, offers a means to reduce uncertainties of the model initial conditions of the aerosol fields. Despite wide use of variational DA techniques in most operational numerical weather prediction (NWP) centers [e.g., Parrish and Derber, 1992; Rabier *et al.*, 2000; Lorenc *et al.*, 2000; Gauthier *et al.*, 2007] to assimilate conventional meteorological observations, satellite retrieval products [e.g., Bormann and Thépaut, 2004], and direct satellite radiances [e.g., Derber and Wu, 1998; McNally *et al.*, 2000], the assimilation of aerosol observations has only recently garnered attention.

[5] Nonetheless, several studies have focused on aerosol DA. For example, Collins *et al.* [2001] introduced assimilating AVHRR AOD in a three-dimensional (3-D) chemical transport model while studying the INDOEX (Indian Ocean Experiment) aerosols. They used an optimal interpolation (OI) technique initially developed for meteorological applications [Lorenc, 1981]. Since then, several other studies have assimilated satellite-derived aerosol products in global and regional chemical transport models using similar OI techniques [Yu *et al.*, 2003; Generoso *et al.*, 2007; Adhikary *et al.*, 2008]. Additionally, Zhang *et al.* [2008] adopted a two-dimensional variational (2DVAR) approach to assimilate MODIS gridded level 3 AOD products over the global ocean with the Naval Research Laboratory (NRL) Aerosol Analysis and Prediction System (NAAPS). Note that the NRL MODIS level 3 AOD products are generated from NASA MODIS level 2 AOD data [Zhang and Reid, 2006]. Furthermore, Niu *et al.* [2008] used a 3DVAR method to assimilate dust loading retrieved from Chinese geostationary satellite FY-2C into the Chinese Unified Atmospheric Chemistry Environment–Dust (CUACE/Dust) forecast system. More recently, the European Centre for Medium-Range Weather Forecasts (ECMWF) extended its four-dimensional variational (4DVAR) meteorological assimilation system to include an aerosol component [Morcrette *et al.*, 2009; Benedetti *et al.*, 2009; Mangold *et al.*, 2011]. Benedetti *et al.* [2009] adopted the total aerosol mixing ratio as a control variable and made some assumptions to partition the total aerosol mass into mass concentration of individual species. Their application to a 2 year (2003 and 2004) reanalysis using MODIS AOD data showed the analyses were skillful at fitting the observations and improving AOD forecasts.

[6] We note that most of the aerosol DA methods (OI, 2DVAR, and 3DVAR) mentioned above used a two-step process: 2-D AOD or 3-D DM40 (dust particle matter with diameter less than 40 μm) [Niu *et al.*, 2008] is first analyzed

from aerosol observations and then partitioned using a post-processing procedure into 3-D mass concentrations of different aerosol species, making assumptions regarding vertical distribution and relative ratio of individual species' mass to total aerosol mass. We acknowledge that some choices in the design of an aerosol assimilation system are constrained by operational feasibility. In this study, we develop a single-step aerosol DA capability within the National Centers for Environmental Prediction (NCEP) operational Gridpoint Statistical Interpolation (GSI) 3DVAR meteorological DA system [Wu *et al.*, 2002; Kleist *et al.*, 2009] coupled to the Weather Research and Forecasting/Chemistry (WRF/Chem) model [Grell *et al.*, 2005]. We then use this system to assimilate MODIS AOD data while modeling a dust storm that occurred in March 2010 over East Asia. Different from previous studies, the newly developed 3DVAR aerosol DA system uses individual aerosol species of the WRF/Chem built-in GOCART module as “control variables.” Therefore, 3-D mass concentrations of the aerosol species are analyzed in a one-step minimization procedure, obviating the need for a second-step postprocessing required by previous studies. To the best of our knowledge, this is the first attempt to use individual aerosol species as analysis variables in a truly 3DVAR DA system. It should be mentioned that several aerosol assimilation studies based on the Ensemble Kalman Filter (EnKF) technique used individual aerosol species as analysis variables [e.g., Sekiyama *et al.*, 2010, 2011; Schutgens *et al.*, 2010]. Furthermore, Yumimoto *et al.* [2007, 2008] adopted the adjoint model-based 4DVAR method to retrieve dust emission over East Asia using ground-based lidar observations.

[7] Section 2 briefly describes the WRF/Chem model and built-in GOCART aerosol module. Section 3 presents the methodology of aerosol DA, including a description of the aerosol background error covariance (BEC) statistics, MODIS AOD observations, and CRTM-AOD observation operator. The experimental design and impact of AOD assimilation applied to a dust storm are described in section 4 before concluding in section 5.

2. WRF/Chem Model and GOCART Aerosol Module

[8] In this study, the WRF/Chem model was used to predict the transport of aerosols and gaseous chemical species in a limited area domain. WRF/Chem is an “online” model, as the chemistry and meteorological components are fully coupled. Both components use the same transport scheme, horizontal and vertical grid, time step, and physical parameterizations for subgrid-scale transport. The chemistry component consists of dry deposition and several choices for gas phase chemical mechanisms, photolysis processes, and aerosol schemes. Aerosol direct and indirect effects through interaction with radiation, photolysis, and microphysical processes are allowed for certain combinations of aerosol and physical options. WRF/Chem also provides tools to utilize several biogenic and anthropogenic emissions data sets in combination with certain chemistry and aerosol schemes.

[9] For this aerosol DA study with WRF/Chem, we chose the Goddard Chemistry Aerosol Radiation and Transport (GOCART) aerosol scheme [Chin *et al.*, 2000, 2002;

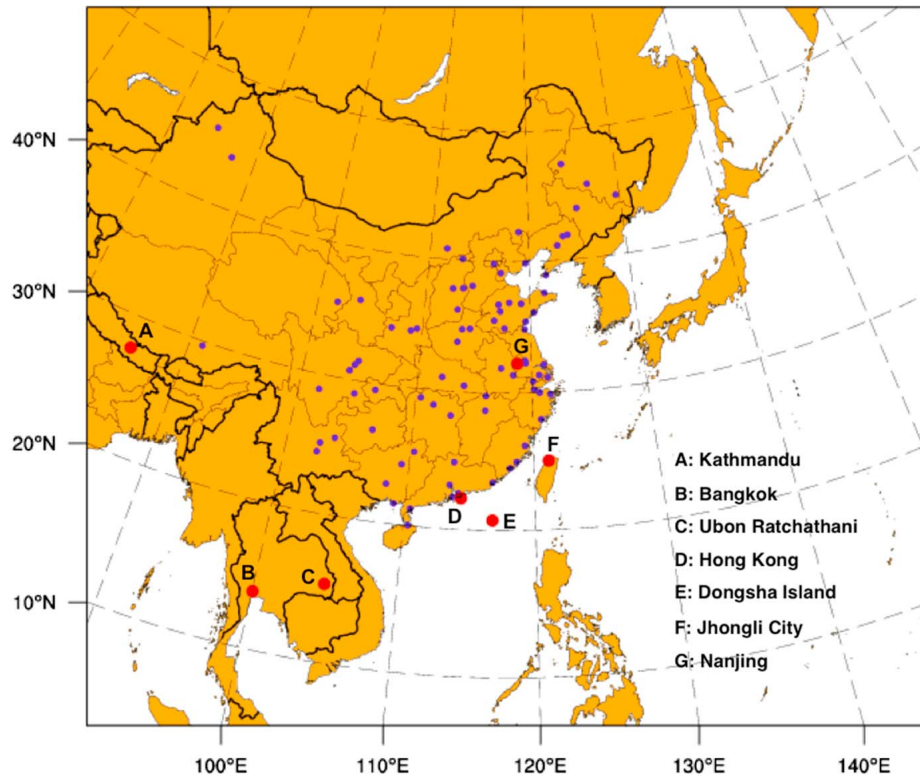


Figure 1. Computational domain. Small dots depict locations where PM_{10} (particulate matter with diameters less than $10\ \mu\text{m}$) verification occurred and large dots with letters indicate Aerosol Robotic Network (AERONET) sites used for aerosol optical depth (AOD) verification. Station identifiers corresponding to the AERONET sites are also listed.

Ginoux et al., 2001] coupled with the Regional Atmospheric Chemistry Mechanism (RACM) [Stockwell et al., 1997] for gaseous chemical mechanism. The GOCART was originally designed as an “offline” global transport model run at low resolution and driven by meteorological fields from the Goddard Earth Observing System Data Assimilation System (GEOS-DAS) [Schubert et al., 1993]. However, now that GOCART has been implemented as an aerosol module within the WRF/Chem model, GOCART numerics can be applied at varying resolution and meteorological fields are simply taken from the WRF/Chem grids.

[10] The GOCART model simulates several tropospheric aerosol types, including sulfate, dust, organic carbon (OC), black carbon (BC), and sea salt. For OC and BC, hydrophobic and hydrophilic components are considered. Many processes regarding the aerosol species’ evolution are represented, including emission, advection, convection, diffusion, dry deposition and wet deposition, as well as chemical reactions using prescribed OH, H_2O_2 , and NO_3 fields for gaseous sulfur oxidations [Chin et al., 2002]. Dry deposition includes sedimentation (gravitational settling) as a function of particle size and air viscosity and surface deposition as a function of surface type and meteorological conditions [Wesely, 1989]. When GOCART is selected as the aerosol module within WRF/Chem, forecasts of 3-D mass concentration of 14 aerosol species are produced: hydrophobic and hydrophilic OC and BC; sulfate; sea salt in four particle size bins (effective radii of 0.3, 1.0, 3.25, and $7.5\ \mu\text{m}$ for dry air)

and dust particles in five particle size bins (effective radii of 0.5, 1.4, 2.4, 4.5, and $8.0\ \mu\text{m}$). The 3-D fields of these 14 aerosol species are central to our implementation of 3DVAR AOD DA (see section 3.2).

[11] To simulate the dust storm that impacted eastern Asia between 19 and 22 March 2010, the WRF/Chem model was run over a computational domain (Figure 1) with 27 km horizontal grid spacing. There were 261 west–east and 222 south–north horizontal grid points and 45 vertical levels. The model top was 50 hPa. The following physical parameterizations [see Skamarock et al., 2008, and references therein] were included: the WRF single-moment 5 class (WSM5) microphysics scheme; the Rapid Radiative Transfer Model (RRTM) longwave and Goddard shortwave radiation schemes; the Mellor–Yamada–Janjic (MYJ) boundary layer scheme; the Noah land surface model; and Grell-3D cumulus parameterization. Lateral boundary conditions (LBCs) for meteorological fields were provided by the NCEP Global Forecast System (GFS). Aerosol and chemical initial conditions (ICs) and LBCs came from the National Center for Atmospheric Research (NCAR) global CAM-Chem model [Lamarque et al., 2005]. The online calculation of biogenic emissions using the U.S. Geological Survey (USGS) land use classification was adopted as by Simpson et al. [1995] and Guenther et al. [1994]. Two anthropogenic emissions inventories were used: gaseous chemistry emissions from the global ($0.5^\circ \times 0.5^\circ$) RETRO (REanalysis of the TROpospheric chemical composition over the past

40 years) inventory (<http://retro.enes.org/>) and gridded $0.5^\circ \times 0.5^\circ$ aerosol emissions from an Asia emissions inventory [Streets *et al.*, 2003; Zhang *et al.*, 2009]. The dust emission flux is computed as a function of probability source function and surface wind speed [Ginoux *et al.*, 2001]. Similar to dust uplifting, sea salt emissions from the ocean are highly dependent on the surface wind speed and calculated as a function of wind speed at 10 m and sea salt particle radius [Chin *et al.*, 2002].

3. Methodology of Aerosol Data Assimilation

3.1. Formulation of Three-Dimensional Variational Data Assimilation

[12] Following the vector–matrix notation of Ide *et al.* [1997], consider a state vector \mathbf{x} of dimension m and an observation vector \mathbf{y} of dimension p (usually $p \ll m$). At a given time, \mathbf{x} and \mathbf{y} are connected by an observation operator H ,

$$\mathbf{y} = H(\mathbf{x}) + \varepsilon_o, \quad (1)$$

where ε_o is an observation error vector. In a meteorological DA framework, \mathbf{x} usually consists of various atmospheric variables such as temperature, humidity, and wind. The observation operator can be a simple horizontal or vertical interpolation from the model grid points to irregular observation locations for those observations that directly measure the model state variables. However, for certain observation types, H can be a complex and highly nonlinear transformation from the model variables to indirect measurements, such as satellite radiances.

[13] In addition to observations, we also possess “a priori” information about \mathbf{x} , which usually comes from a short-range NWP model forecast and is commonly referred to as the background (\mathbf{x}_b) with

$$\mathbf{x}_b = \mathbf{x} + \varepsilon_b, \quad (2)$$

where ε_b is the background error vector. The goal of DA is to find a best estimate of \mathbf{x} , the analysis, given the observations and background to initialize a NWP model forecast.

[14] To find a best estimate of \mathbf{x} in the sense of minimum analysis error variance, a 3DVAR algorithm [Lorenc, 1986; Parrish and Derber, 1992; Rabier *et al.*, 1998] is employed. A 3DVAR DA technique minimizes a cost function (J) that measures the distance of the state vector to the background and observations, given by

$$J(\mathbf{x}) = \frac{1}{2}(\mathbf{x} - \mathbf{x}_b)^T \mathbf{B}^{-1}(\mathbf{x} - \mathbf{x}_b) + \frac{1}{2}[H(\mathbf{x}) - \mathbf{y}]^T \mathbf{R}^{-1}[H(\mathbf{x}) - \mathbf{y}], \quad (3)$$

where \mathbf{B} and \mathbf{R} are the background and observation error covariance matrices of dimensions $m \times m$ and $p \times p$, respectively. \mathbf{B} and \mathbf{R} determine the relative contributions of the background and observation terms to the final analysis. As \mathbf{x} and \mathbf{y} are column vectors, $J(\mathbf{x})$ is simply a scalar.

[15] Most operational NWP centers adopt an incremental implementation [Courtier *et al.*, 1994] of equation (3),

$$J(\delta\mathbf{x}) = \frac{1}{2}\delta\mathbf{x}^T \mathbf{B}^{-1}\delta\mathbf{x} + \frac{1}{2}(\mathbf{H}\delta\mathbf{x} - \mathbf{d})^T \mathbf{R}^{-1}(\mathbf{H}\delta\mathbf{x} - \mathbf{d}), \quad (4)$$

where the analysis depends on the “increment,” $\delta\mathbf{x}$ ($\delta\mathbf{x} = \mathbf{x} - \mathbf{x}_b$), and “innovation vector,” \mathbf{d} [$\mathbf{d} = \mathbf{y} - H(\mathbf{x}_b)$], the

difference between the observation and background]. \mathbf{H} is the linearized version (or Jacobian, a $p \times m$ matrix) of the nonlinear observation operator H in the vicinity of \mathbf{x}_b . $J(\delta\mathbf{x})$ is minimized when its gradient (the first-order partial derivative) with respect to $\delta\mathbf{x}$ is equal to zero, i.e.,

$$\nabla J_{\delta\mathbf{x}} = \mathbf{B}^{-1}\delta\mathbf{x} + \mathbf{H}^T \mathbf{R}^{-1}(\mathbf{H}\delta\mathbf{x} - \mathbf{d}) = 0. \quad (5)$$

For most current NWP models, the dimension m is usually on the order of 10^7 and it is impossible to invert the very large matrix \mathbf{B} and solve equation (5) analytically. Thus, an iterative minimization algorithm [Navon and Legler, 1987] is typically used to find the minimum of $J(\delta\mathbf{x})$.

[16] Our development for MODIS AOD DA is based upon the NCEP GSI analysis system. The use of recursive filters in GSI permits a spatially inhomogeneous BEC matrix \mathbf{B} [Wu *et al.*, 2002]. Only standard deviation and horizontal and vertical length scales of the background error for GSI analysis variables are needed to apply recursive filters both horizontally and vertically. Originally, a preconditioned conjugate gradient minimization algorithm [Derber and Rosati, 1989] was implemented in GSI. However, a recent GSI version also contains a variable storage quasi-Newton algorithm [Gilbert and Lemaréchal, 1989] that was used in our AOD DA experiments. Sections 3.2–3.4 detail our extension of GSI to assimilate AOD.

3.2. Aerosol Analysis Variables and the Background Error Covariance Statistics

[17] For our implementation of AOD DA, the 3-D mass concentrations of the 14 WRF/Chem GOCART aerosol species within the entire domain and at all model levels comprised the analysis variables (or “control variables”) in the GSI 3DVAR minimization procedure. Since we assimilated only AOD to analyze the 3-D mass concentration of 14 aerosol species, the 3DVAR problem defined here is under constrained in the sense of observational information content. However, the problem is well constrained in the mathematical sense because of the use of prior information from the model background.

[18] As individual aerosol species were the analysis variables, it was necessary to calculate BEC statistics for each aerosol variable. We accomplished this task by using the NMC method [Parrish and Derber, 1992], which calculates BECs by taking differences between forecasts of different lengths valid at common times. While the NMC method is typically used to produce BECs for traditional meteorological fields (e.g., wind, temperature), it can be applied to forecasts of mass concentration of aerosol species [Benedetti and Fisher, 2007; Benedetti *et al.*, 2009]. Differences of 24 and 12 h WRF/Chem forecasts of the aerosol species valid at the same time for 62 pairs valid at either 00:00 and 12:00 UTC over the whole month of March 2010 were used to compute the aerosol BECs. ICs and LBCs for each forecast came from the NCAR global CAM-Chem model. In this first implementation, no cross correlation between different aerosol variables was considered because of the incapability of the current GSI 3DVAR to directly model the cross correlation in the \mathbf{B} matrix. In the future, cross correlation of aerosol species could be introduced using the hybrid variational/ensemble technique [Wang *et al.*, 2008]. Standard deviations and horizontal and vertical length scales

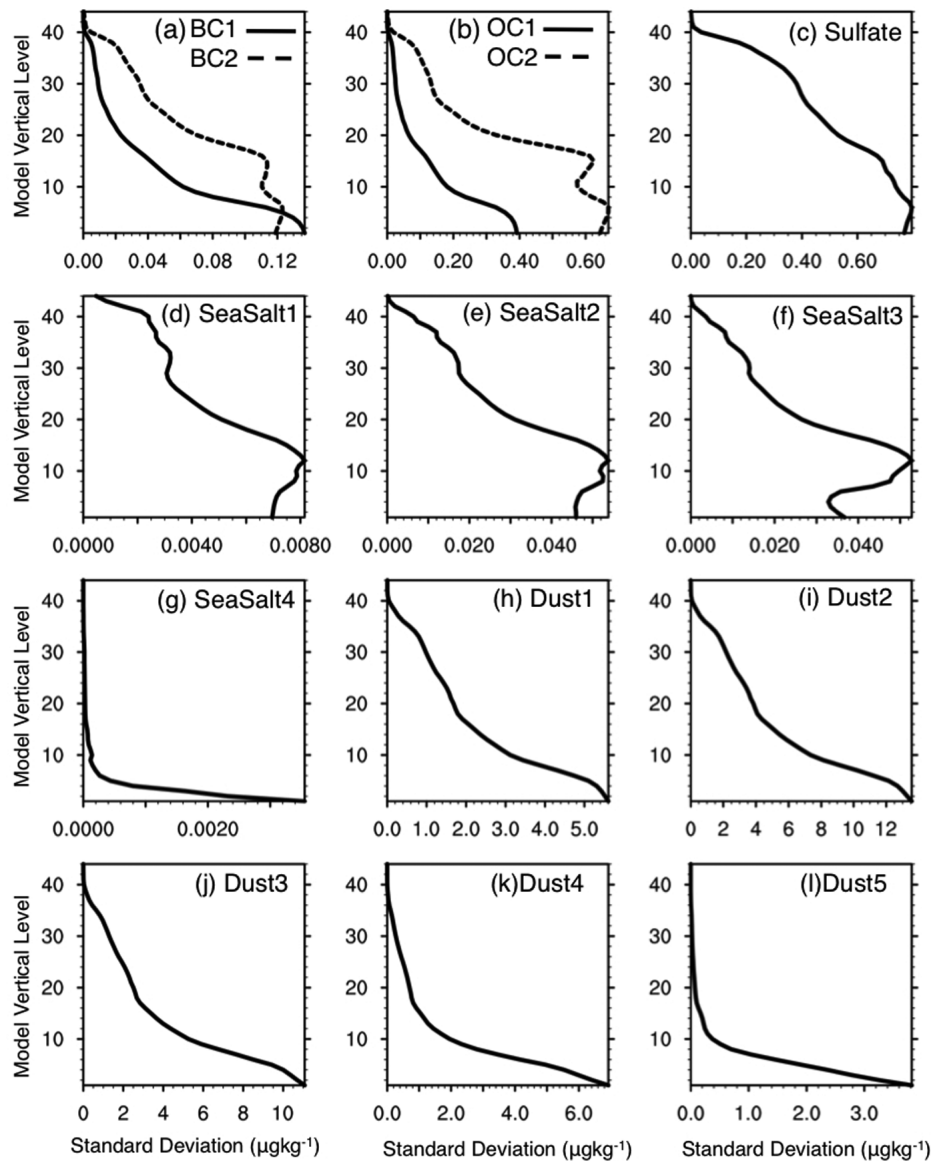


Figure 2. Domain-averaged background error standard deviation (μgkg^{-1}) for each model level (y axis) for (a) BC1 (solid line) and BC2 (dashed line), (b) OC1 (solid line) and OC2 (dashed line), (c) sulfate, (d–g) sea salt aerosol species with different effective diameters (see text and Table 1), and (h–l) dust aerosol species (see text and Table 1).

for each aerosol variable were calculated using the method described by *Wu et al.* [2002].

[19] The domain average standard deviations and horizontal length scales at each model level are shown for all 14 species in Figures 2 and 3. Standard deviations varied substantially across the species, spanning several orders of magnitudes, which corresponded to different magnitude of the species' mass concentrations. *Benedetti and Fisher* [2007] also used the NMC method to calculate BEC statistics for the sum of the mixing ratios of all aerosol species from the ECMWF global model. The shape of the standard deviation profile in their statistics [*Benedetti and Fisher*, 2007, Figure 3a] is consistent with our statistics for dust.

[20] The values of the horizontal length scale were comparable for all the species, generally spanning ~ 1.5 –

2.5 times the grid spacing, consistent with the statistics reported by *Kahnert* [2008], who used an offline transport model at 0.4° resolution over Europe. However, the vertical variation of the horizontal length scale differs among the species. The vertical patterns are seemingly related to the particle size. For instance, fine mode species such as SeaSalt1, SeaSalt2, DUST1, and DUST2 exhibit similar vertical structures of the horizontal length scales.

3.3. MODIS Aerosol Optical Depth Retrieval Product

[21] AOD data from MODIS sensors on board Terra and Aqua satellites are widely used in aerosol studies. For this study, we used the most recent release (collection 051) of level 2 total AOD retrievals from both Terra and Aqua. To maximize the observation coverage within ± 3 h data

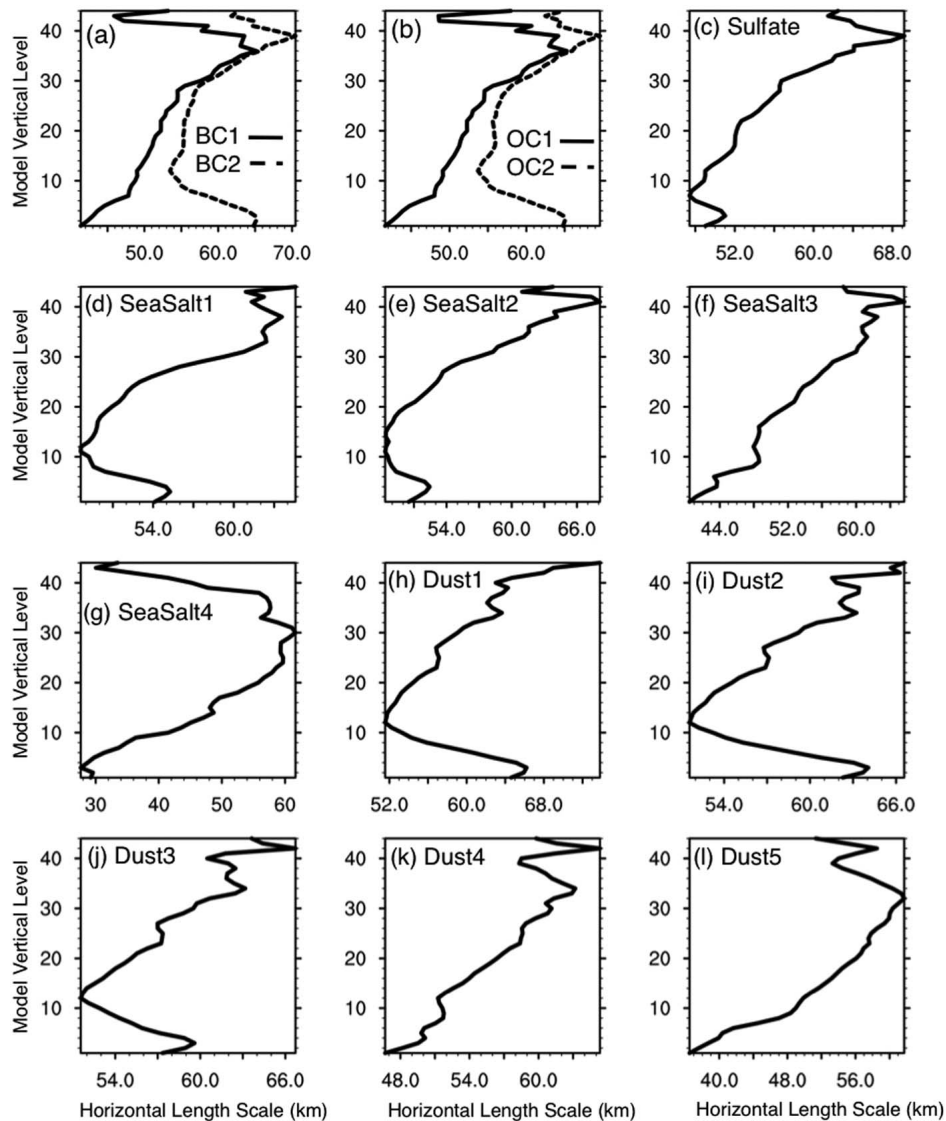


Figure 3. As in Figure 2 except domain-averaged background error horizontal correlation length scale (km) for each model level.

assimilation time window, we used AOD retrievals over land and sea derived from the dark target product [Remer *et al.*, 2005] and “deep blue” product over bright land surface [Hsu *et al.*, 2004, 2006]. The dark target ocean and land AOD products were available from both Terra and Aqua, but deep blue retrievals were only available from Aqua. MODIS retrieved AOD was provided at seven wavelengths: 470, 550, 660, 870, 1240, 1630, and 2130 nm. However, only the optical depth at 550 nm was assimilated in this study.

[22] MODIS AOD products are in HDF-EOS format and separated by “granules” (a 5 min segment of the satellite’s orbit). However, GSI requires observations in BUFR format. Therefore, the original AOD products were combined and converted from the 5 min granules into a single file within the DA time window and domain in NCEP BUFR format. We used a simple observation error specification suggested by Remer *et al.* [2005], who separately estimated the AOD

retrieval uncertainty over both ocean (5% of AOD value) and land (15% of AOD value). Only AOD retrievals marked with the best quality flag were assimilated. The original MODIS AOD level 2 products are at 10 km \times 10 km resolution but the observations were thinned to the same resolution as the model grid. Model aerosol fields were interpolated to observation locations before applying the AOD observation operator described in section 3.4.

[23] In our domain, MODIS AOD products provided coverage only at 00:00 and 06:00 UTC (daytime) with generally only Terra at 00:00 UTC, and both Terra and Aqua at 06:00 UTC with more coverage. Figure 4 shows the AOD coverage within a ± 3 h time window centered at 06:00 UTC on 21 March 2010. Most data were distributed in southern and eastern parts of the domain and the deep blue product from Aqua had sparse coverage over Mongolia and northwestern China, typical source regions of Chinese dust storms.

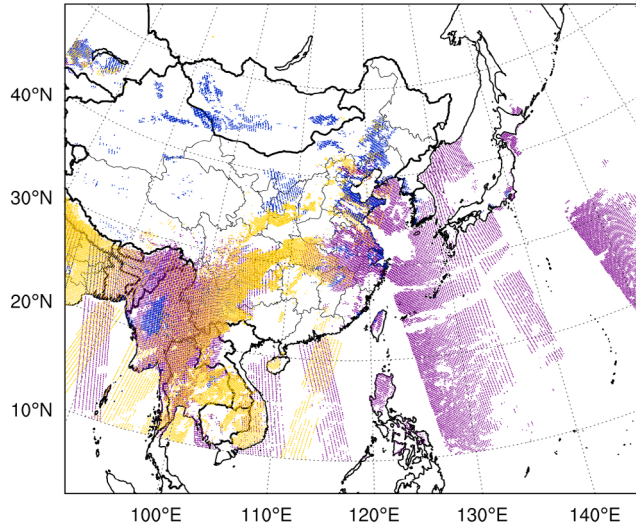


Figure 4. Moderate Resolution Imaging Spectroradiometer (MODIS) AOD coverage from the Aqua and Terra satellites at 06:00 UTC 21 March 2010. Purple: dark surface retrievals from Aqua; gold: dark surface Terra; blue: deep blue produced from Aqua.

3.4. AOD Observation Operator

[24] The AOD observation operator is based upon the community radiative transfer model (CRTM) [Han *et al.*, 2006; Liu and Weng, 2006], developed at the United States Joint Center for Satellite Data Assimilation (JCSDA). The CRTM was primarily designed for computing satellite radiances and is used in GSI for directly assimilating radiances from infrared and microwave sensors. We extended the CRTM to compute MODIS AOD using only aerosol profiles as input. This newly developed CRTM-AOD module was incorporated into the GSI system. Some implementation details are described below.

[25] Aerosols can scatter and absorb radiation. The absorption and scattering depends on the size distributions and refractive indices of the aerosols. In this study, we assumed spherical aerosol particles. The aerosol size distribution may have multiple modes. For each mode, a typical aerosol size function is assumed to be the lognormal distribution [d'Almeida *et al.*, 1991] for N particles within the mode,

$$n(\ln r) = \frac{N}{\sqrt{2\pi} \ln(\sigma_g)} \exp \left[-\frac{1}{2} \left(\frac{\ln r - \ln r_g}{\ln(\sigma_g)} \right)^2 \right], \quad (6)$$

where r is a radius, r_g the geometric median radius, and σ_g the geometric mean standard deviation. The k th moment (M_k) of the distribution can be expressed as [Binkowski and Roselle, 2003]

$$M_k = \int_{-\infty}^{\infty} r^k n(\ln r) d \ln(r) = r_g^k \exp \left[\frac{k^2}{2} \ln^2(\sigma_g) \right]. \quad (7)$$

M_0 is the number (N) of aerosol particles. M_2 and M_3 are proportional to the total particulate surface area and volume, respectively. The effective radius (r_{eff}) is defined as

$$r_{eff} = \frac{M_3}{M_2} = r_g \exp \left[\frac{5}{2} \ln^2(\sigma_g) \right]. \quad (8)$$

For sulfate, sea salt, and hydrophilic OC and BC, water uptake effects need to be included. The particle size increases as relative humidity of the ambient atmosphere increases. The refractive index is calculated by considering aerosol water content. The effective radius growth factor for hygroscopic aerosols may be theoretically calculated or obtained from a precalculated look-up table [Chin *et al.*, 2002]. Once the growth factor (a_g) is evaluated, the refractive index (n_r) for the hygroscopic aerosol can be calculated using a volume mixing method as

$$n_r = n_w + (n_o - n_w) \times a_g^3, \quad (9)$$

where n_o and n_w are the refractive indices for dry aerosols and water, respectively. We adopted refractive indices n_o from the software package of Optical Properties of Aerosols and Clouds (OPAC) [Hess *et al.*, 1998]. The water refractive index is given by Hale and Querry [1973].

[26] After the size distribution and refractive index were computed, we applied Mie scattering code [van de Hulst, 1957] to compute mass extinction coefficient ext ($m^2 g^{-1}$), single scattering albedo, and phase function. Finally, AOD for each aerosol type i at the j th atmospheric layer for a wavelength λ was calculated as

$$\tau_{ij}(\lambda) = ext(\lambda, i, r_{eff}) \times c_{ij}, \quad (10)$$

where c_{ij} is aerosol column mass in g/m^2 . It can be seen from equation (10) that the AOD depends linearly on the layer column aerosol mass. The column total AOD is a sum of equation (10) over all aerosol types and atmospheric layers. In addition to the AOD forward model, the Jacobian of AOD with respect to aerosol mass concentration was also derived, which was required to calculate the gradient of the cost function (equation (5)) in the 3DVAR analysis. As well as outputting AOD at MODIS wavelengths, the CRTM-AOD

Table 1. Goddard Chemistry Aerosol Radiation and Transport (GOCART) Aerosol Optical Properties at 550 nm for Dry Air

Aerosol Type	Density ($g\ cm^{-3}$)	Effective Radius (μm)	Standard Deviation (μm)	Mass Extinction Coefficient ($m^2\ g^{-1}$)
Sulfate	1.7	0.242	2.03	3.13
OC1 (hydrophobic)	1.8	0.087	2.20	2.65
OC2 (hydrophilic)	1.8	0.087	2.20	2.65
BC1 (hydrophobic)	1	0.036	2.0	9.16
BC2 (hydrophilic)	1	0.036	2.0	9.16
SeaSalt1	2.2	0.3	2.03	2.59
SeaSalt2	2.2	1.0	2.03	0.90
SeaSalt3	2.2	3.25	2.03	0.24
SeaSalt4	2.2	7.5	2.03	0.097
Dust1	2.6	0.5	2.0	1.61
Dust2	2.6	1.4	2.0	0.51
Dust3	2.6	2.4	2.0	0.27
Dust4	2.6	4.5	2.0	0.14
Dust5	2.6	8.0	2.0	0.076

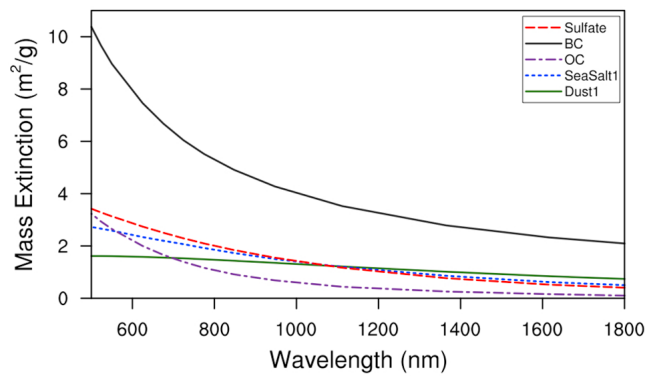


Figure 5. Mass extinction coefficient as a function of wavelength for five aerosol species listed in Table 1.

operator can also calculate AOD at wavelengths (500, 675, 870, 1020, and 1640 nm) required to validate forecasts with retrieved AODs from AERONET [Holben *et al.*, 1998].

[27] AOD also depends linearly on the extinction coefficient, which is a function of wavelength, aerosol type and particle effective radius. Table 1 gives effective radius and mass extinction coefficients at 550 nm of the 14 GOCART aerosol variables for dry air. At visible wavelengths, the mass extinction coefficient generally decreases as the size of natural aerosols increases. Figure 5 depicts mass extinction coefficient as a function of wavelength for five aerosol species listed in Table 1. The wavelengths in the plot span 500–1800 nm, covering the observations' spectrums used in this paper, either for DA or validation purposes. Extinction by DUST1 displays a flat spectral signature and BC extinction rapidly decreases from 500 to ~ 850 nm, but decreases more slowly at longer wavelengths. These spectral characteristics aid determination of the composition of aerosol types at different locations.

4. Application to a Dust Storm

[28] A dust storm that started in Mongolia blasted Beijing on 20 March 2010 and covered large areas of China in the following days. Several countries in East Asia were affected. Hong Kong, Taiwan, Japan, and South Korea recorded extremely poor visibility and air quality was hazardous to human health. A number of residents reported health problems, while flights were canceled or delayed because of poor visibility caused by dust. The dust was lofted by strong winds accompanying a cold front that crossed China on 20 March. The winds passed over regions of Mongolia and northwest China that had been suffering from an extended drought. PM_{10} measurements in Beijing reached maximum values of $\sim 800 \mu\text{g}/\text{m}^3$ on 20 March. AOD (500 nm) values observed at the Nanjing AERONET site varied from less than 1 on 19 March to a maximum of ~ 2 on 21 March. Average MODIS AOD values over most of China varied from less than 0.5 on 18 March to more than 0.9 on 20–21 March, when eastern China was severely affected by the dust storm.

4.1. Experimental Design

[29] Two parallel experiments were designed to evaluate the impact of MODIS AOD DA on analyses and forecasts of

aerosols over eastern Asia. One experiment served as the control and did not employ any DA, while AOD DA was implemented in the other. Each experiment initialized a new WRF/Chem forecast every 6 h between 00:00 UTC 17 March and 00:00 UTC 24 March 2010 (inclusive). All forecasts were integrated for 6 h and hourly model output was archived. Every initialization, both experiments' meteorological fields were updated by interpolating GFS analyses onto the computational domain. Gaseous chemical variables were initialized from the previous cycle's 6 h forecast, except for the first forecast (00:00 UTC 17 March), when gaseous and aerosol ICs came from NCAR global CAM-Chem model output.

[30] The two experiments only differed regarding initialization of the 14 WRF/Chem-GOCART aerosol species contained in the GSI analysis. In the experiment without DA, the GOCART aerosol fields were simply initialized from the previous cycle's 6 h forecast. However, the experiment that employed DA performed a 3DVAR aerosol analysis before each new initialization beginning 06:00 UTC 17 March, using the GOCART aerosol fields from the previous cycle's 6 h forecast as the background. The subsequent WRF/Chem forecasts were initialized with the updated aerosol fields, the meteorological fields from the GFS analyses, and gaseous chemistry fields inherited from the previous cycle's 6 h forecast. Thus, the experiments only differed in that 3DVAR DA updated the profiles of GOCART aerosol species in one experiment but not the other, permitting a clear isolation of the impact of cyclic AOD DA. Both experiments used the same WRF/Chem physical and chemistry options outlined in section 2.

[31] Note that MODIS AOD data were only present during the day (00:00 and 06:00 UTC), and therefore, the aerosol fields valid at 00:00 UTC should be considered as 18 h forecasts initialized at 06:00 UTC the previous day, since no AOD observations were present at 12:00 or 18:00 UTC to update aerosol fields. However, meteorological fields were still updated from GFS analyses at 12:00 and 18:00 UTC. The analyses and forecasts from the two experiments were compared to AOD observations from MODIS, AERONET, and CALIOP, as well as surface PM_{10} (particulate matter with diameters less than $10 \mu\text{m}$) observations.

4.2. Results

4.2.1. Comparison to MODIS AOD

[32] Figure 6 displays the time series of domain-averaged bias (Figure 6a) and root-mean-square error (RMSE) (Figure 6b) of WRF/Chem forecasts and GSI analyses of AOD when compared to MODIS AOD observations. These statistics served as "sanity checks" to determine whether the aerosol assimilation algorithm worked properly and assess the quality of the first guess. Only times valid at 00:00 and 06:00 UTC, when MODIS AOD data were present, are plotted for the period of 18–23 March 2010. Dotted green curves show the errors of 6 h forecasts from the control experiment without AOD DA (NoDA) and blue solid lines represent errors of 6 h forecasts (which also served as the background fields for AOD DA) from the AOD DA experiment. Analysis errors after AOD DA are given by dashed black curves.

[33] Both bias and RMSE give the same indication regarding performance of the DA and NoDA experiments.

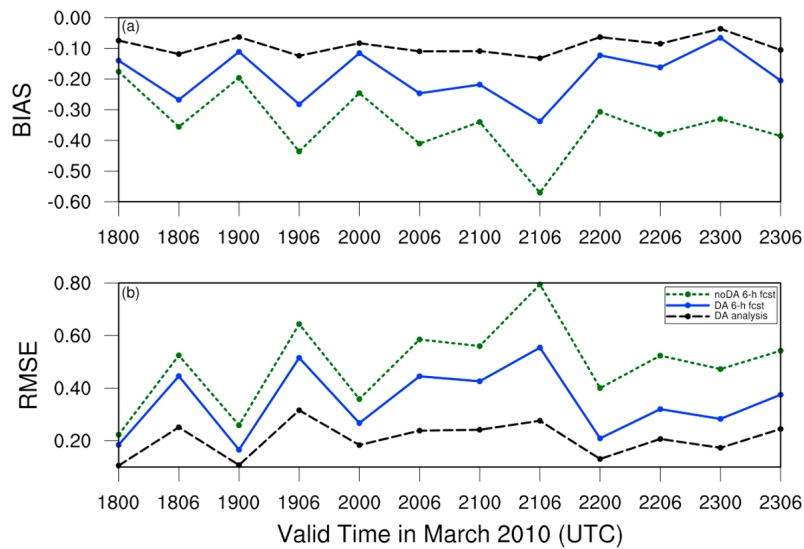


Figure 6. Time series of domain-averaged (a) bias and (b) root-mean-square error (RMSE) of AOD Weather Research and Forecasting/Chemistry model forecasts and Gridpoint Statistical Interpolation aerosol analyses. The x axis labels combine date and hour (DDHH). Only times valid at 00:00 UTC and 06:00 UTC, when MODIS AOD data were present, are plotted for the period of 18–23 March 2010 (section 4.2.1).

From the NoDA experiment, it is clear that the WRF/Chem model underpredicted AOD (biases of -0.2 to -0.6), especially at 06:00 UTC 21 March, when the dust storm reached its maximum intensity in eastern China. The magnitude of bias and RMSE from WRF/Chem appears to be similar to that reported by *Morcrette et al.* [2009] for AOD forecast error statistics over Southeast Asia in April 2003. They ran free forecasts of aerosols with the ECMWF global model and verified forecasts against AERONET AOD observations.

[34] After AOD DA, the model low bias was substantially reduced, with bias (RMSE) values consistently near -0.1 (0.2). Overall, the bias and RMSE were reduced an average of $\sim 20\%$ compared to the NoDA experiment during the dust storm period. Interestingly, the model output more closely agreed with MODIS AOD observations valid at 00:00 UTC than at 06:00 UTC, even though forecasts valid at 00:00 UTC had longer effective forecast lead times, as discussed above. This behavior likely occurred because MODIS data at 00:00 UTC covered mostly the western Pacific Ocean, where AOD retrievals have less uncertainty than over land [*Remer et al.*, 2005].

[35] Figure 7a shows 550 nm MODIS AOD observations assimilated during the 06:00 UTC 21 March analysis. The horizontal AOD distributions from model output at 06:00 UTC 21 March are displayed in Figures 7b, 7c and 7d, respectively, for the NoDA experiment and the analysis and background (i.e., 6 h forecast from previous cycle's analysis) from the DA experiment. Consistent with Figure 6, the DA experiment produced larger AOD values than the NoDA experiment and agreed more closely with MODIS observations. In the eastern AOD band, few good observations were available for assimilation and larger AOD values in the DA experiment resulted from previous assimilation/forecast cycles. Large differences between the NoDA and DA experiments also occurred over southeast China, Vietnam, Laos and Thailand, where AOD values increased after

assimilation and fit more closely to MODIS observations than the background. Even though few observations were assimilated over some regions (southeast China and Vietnam) of this area, analysis increments were generated, indicating the capability of our data assimilation system to transfer observational information to nearby regions with sparse observation coverage through the background error spatial correlation.

4.2.2. Comparison Between the Background and Analysis for Each Aerosol Variable

[36] A two-step approach for aerosol analysis (see section 1) usually requires assumptions and constraints to partition the first-step AOD analysis into profiles of individual aerosol species in the second step. For instance, *Zhang et al.* [2008] adopted a simple scaling technique for all species by assuming the relative ratio of each aerosol species' mass concentration to the total aerosol mass concentration was constant before and after the analysis. However, this assumption can be problematic if the background field is bad. Our one-step 3DVAR aerosol analysis does not apply any constraints regarding relative ratio of each species' mass concentration to the total aerosol mass concentration. The main constraints in our system were the specification of the observation and background error covariances.

[37] It is interesting to see how our assimilation method impacted the analyses of individual aerosol species. Figure 8 shows domain-averaged total aerosol mass concentration (Figure 8a) and the species' relative contribution to the total mass (in terms of percentage; see Figures 8b–8f) before (solid lines) and after (dotted lines) AOD DA for each model level at 06:00 UTC 21 March. Only species whose concentrations increased after DA (BC1/2, OC1/2, and DUST1/2/3) are shown in Figure 8. Mass concentrations of Sulfate, DUST4, DUST5, and all sea salt species were nearly unchanged by AOD DA (not shown).

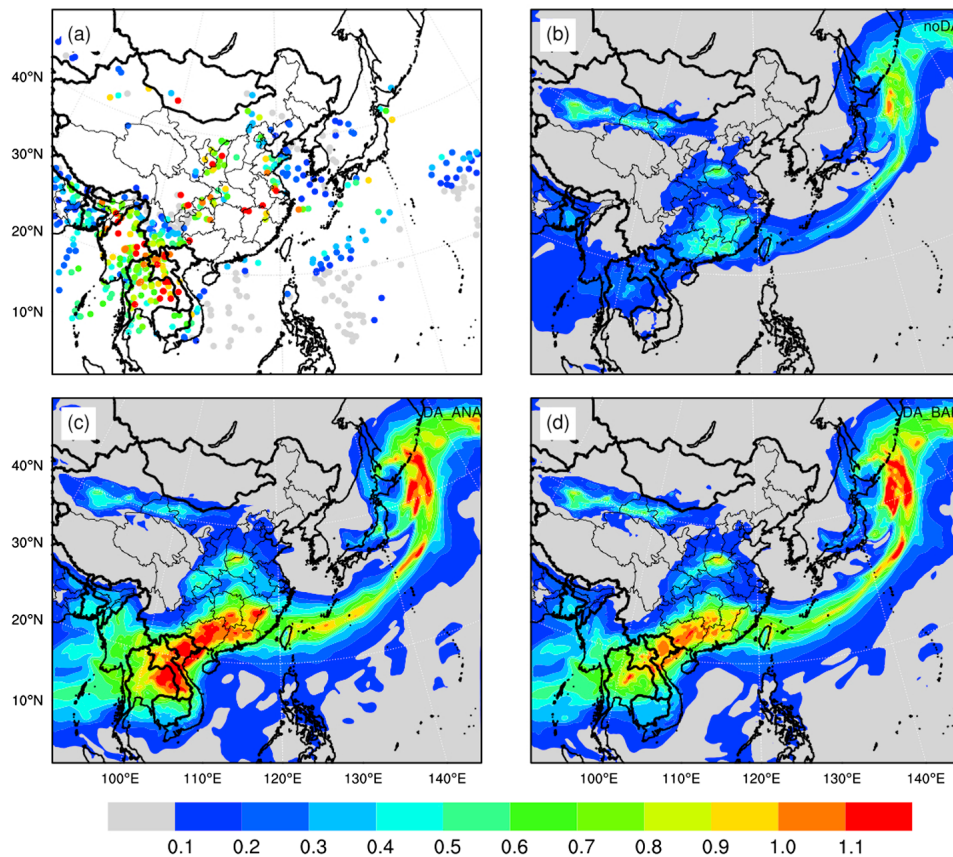


Figure 7. (a) 550 nm MODIS AOD observations assimilated within the ± 3 h data assimilation window for the 06:00 UTC 21 March analysis and the corresponding model output at 06:00 UTC 21 March for the (b) control experiment without AOD data assimilation (NoDA) experiment and the (c) analysis and (d) background (i.e., 6 h forecast from the previous cycle's analysis) from the AOD DA experiment.

[38] The total aerosol mass concentration was increased after AOD DA (Figure 8a), thus, reducing the low model bias while preserving the shape of the profile. The profile shapes of the individual species (Figures 8b–8f) also were preserved, which was expected, since total AOD provides no vertical information about aerosol optical properties. At the lowest model level, the total mass concentration of the analysis increased 15% over the background for this case. Even though all species shown in Figure 8 had increased concentrations after AOD DA, the relative ratios of individual species' mass concentration to the total mass concentration differed across the species. Relative ratios of OC2, DUST1, and DUST2 increased in the analysis, representing a relatively large increase of mass concentration for these species. On the other hand, BC1, BC2, OC1, and DUST3 ratios decreased after DA because of a relatively small increase of their mass concentrations. It is hard to determine whether this behavior is preferable because of the lack of available validation data for individual species. However, when examining several AERONET AOD observations within the domain, we found that fine mode AOD was dominant and explained $\sim 80\%$ of the total AOD, on average (not shown). Thus, it seems appropriate that fine mode (particle size $< 2 \mu\text{m}$, see Table 1) dust species (i.e., DUST1 and DUST2) contributed most to the total aerosol mass concentration after the analysis.

4.2.3. Comparison to AERONET AOD

[39] The AERONET program, equipped with Sun photometers, is a federation of ground-based remote sensing aerosol networks [Holben *et al.*, 1998]. The Sun photometer measures solar radiation over a number of wavelengths in the absence of cloudiness. AOD is then calculated from these measurements. During the period of this study, AOD observations were available at seven AERONET sites (see Figure 1) and used for validating AOD forecasts and analyses. In order to validate AOD at AERONET specific wavelengths, the CRTM-AOD operator was modified to include the AOD calculation for those wavelengths.

[40] Figure 9 depicts the hourly time series of AOD at 500 nm for the whole experimental period (00:00 UTC 17 through 06:00 UTC 24 March) at six AERONET sites in the domain. Among those sites, Nanjing, Jhongli of Taiwan, and Hong Kong were affected by the dust storm. The analyzed AOD values after DA are shown only at 00:00 and 06:00 UTC, when MODIS AOD data were present. Otherwise, hourly model forecast output is displayed. The NoDA experiment (green lines) produced AOD values far below AERONET observations (red lines), but assimilating MODIS AOD (blue lines) yielded AOD values much closer to AERONET observations, although to different extents among the sites and dates. The peak AOD values in Nanjing around 06:00 UTC 21 March (Figure 9a), during the dust

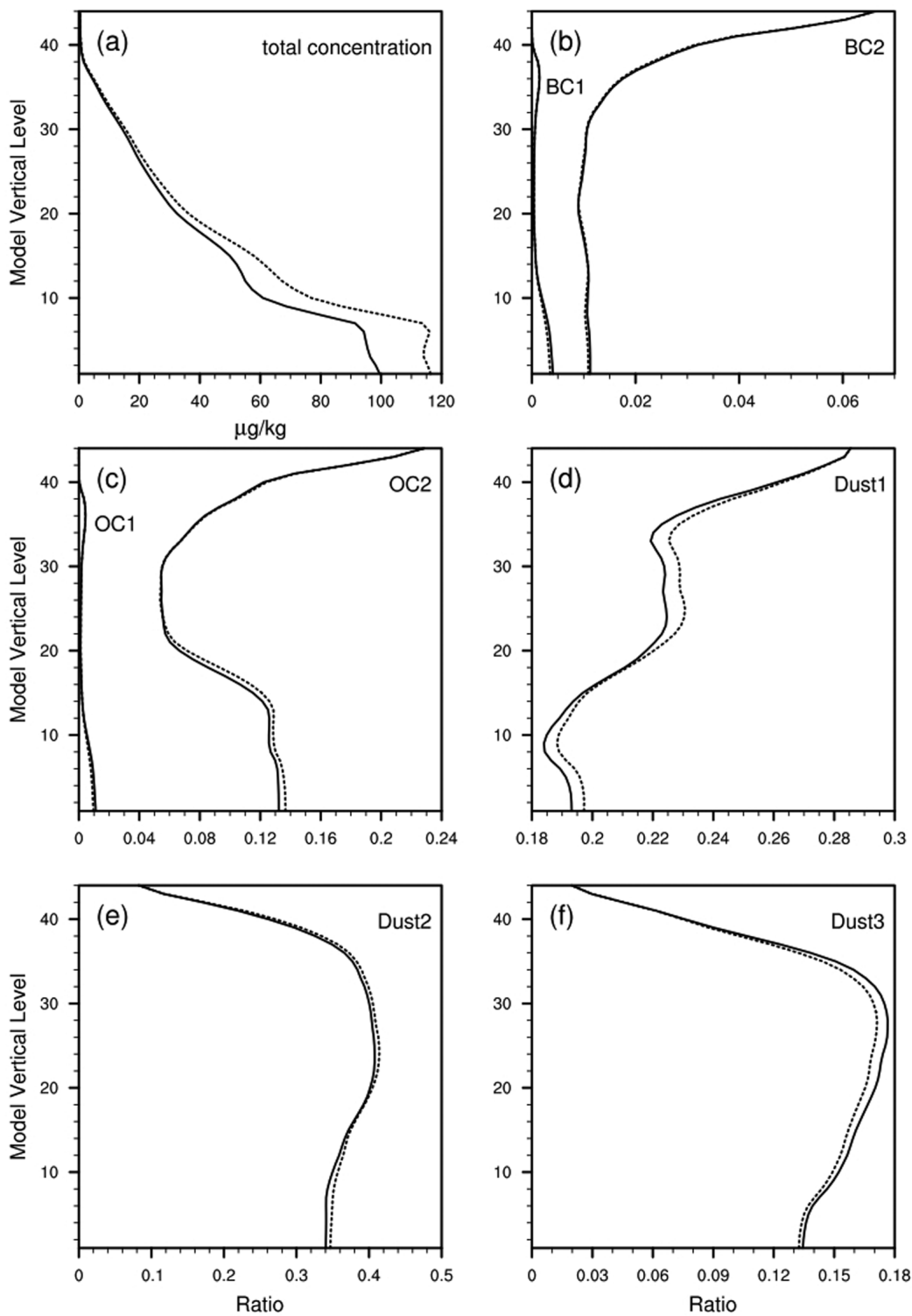


Figure 8. (a) Domain-averaged total aerosol mass concentration ($\mu\text{g}/\text{kg}$) and ratio of mass concentration of (b) BC1 and BC2, (c) OC1 and OC2, (d) DUST1, (e) DUST2, and (f) DUST3 to the total aerosol mass concentration before (solid lines) and after (dotted lines) AOD DA for each model level at 06:00 UTC 21 March. The model levels 10, 20, 30, and 40 correspond to heights (from sea level over water) of about 1.3, 3.9, 7.5, and 14 km.

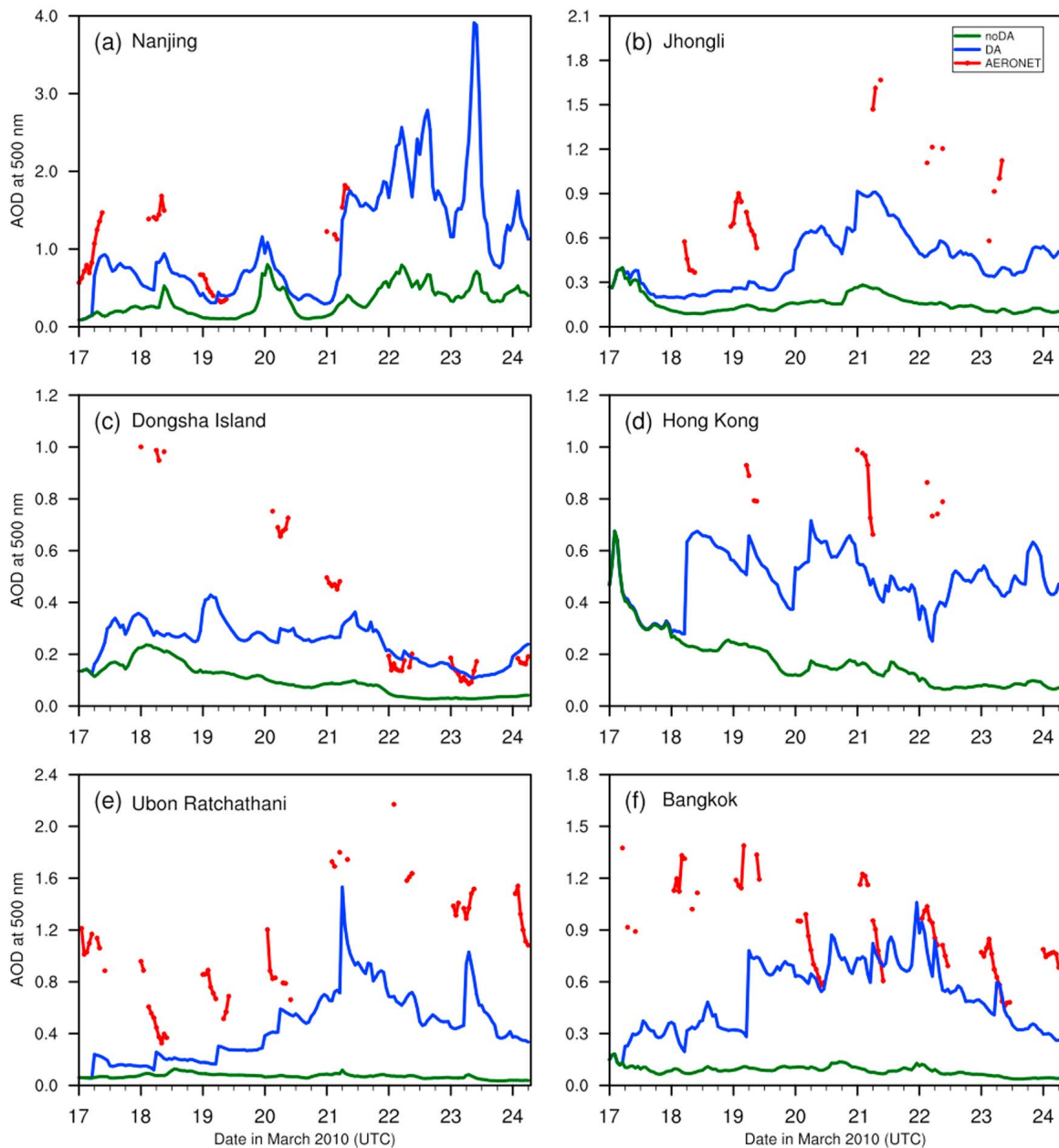


Figure 9. Hourly time series of total AOD at 500 nm from 00:00 UTC 17 March to 06:00 UTC 24 March at AERONET sites in (a) Nanjing, (b) Jhongli city of Taiwan, (c) Dongsha Island, (d) Hong Kong, (e) Ubon Ratchathani, and (f) Bangkok. Model output is hourly. Red line denotes the AERONET observations, and blue and green curves represent the DA and NoDA experiments, respectively.

storm, were simulated accurately by the DA experiment. AOD DA's capability to capture the extreme event around 06:00 UTC 21 March was also evident in Ubon Ratchathani (Figure 9e). The decrease of AOD values beginning 22 March in Dongsha Island was also well depicted in the DA experiment. At early times of the simulation period, AOD values at some sites (e.g., Dongsha Island and Bangkok) were underestimated even with AOD DA, likely because of no coverage of MODIS AOD data.

[41] Figure 10 shows AOD verification at four wavelengths (1640, 1020, 870, and 675 nm) at an AERONET site in Kathmandu, the capital and largest city of Nepal. This

site was unaffected by the dust storm and typical air pollution dominated the AOD. The NoDA experiment severely underestimated AOD compared to the AERONET observations, likely revealing the underestimated emissions from the "Streets" 2006 Asia emissions inventory [Zhang *et al.*, 2009] used for emissions in our study. This issue of underestimated emissions might be unavoidable when applying historical emissions inventories in developing countries with rapidly increasing industrial activities. Zhang *et al.* [2009] investigated the emissions trends of various species in China and found that between 2001 and 2006, SO_2 , NO_x , CO, VOC (Volatile organic compound), and

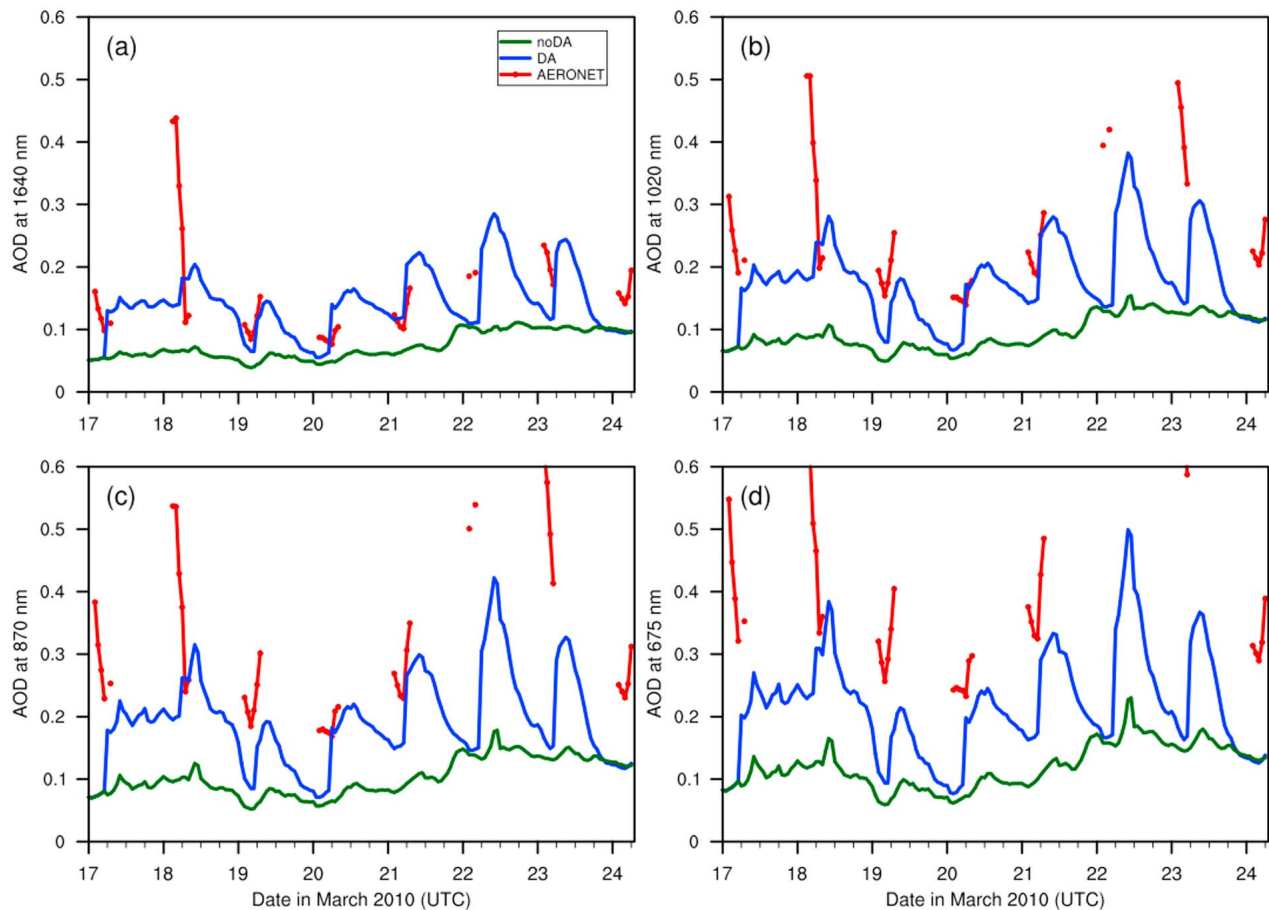


Figure 10. As in Figure 9 but for AOD validation at the Kathmandu AERONET site for four wavelengths: (a) 1640, (b) 1020, (c) 870, and (d) 675 nm.

PM_{10} concentrations increased 36%, 55%, 18%, 29%, and 13%, respectively, while there was a 14% increase for $PM_{2.5}$, BC and OC. However, assimilation of current data provides a method to overcome shortcomings of “climatological” emissions. The AOD values from the DA experiment (blue line) agree more closely with AERONET observations. The minimum AOD values around 06:00 UTC (local noon) were captured, particularly for longer wavelengths (1640 and 1020 nm). Kathmandu is one of the most polluted cities in Asia, partly because of high year-round traffic volume of fuel inefficient vehicles [Sharma, 1997]. The diurnal variation of AOD in the AERONET observations, and replicated by the DA experiment, likely reflects changes in traffic from the morning to evening. The DA experiment agreed less with observations as the wavelength decreased, perhaps because of less accurate analyses and forecasts of certain species more sensitive to shorter wavelengths, which underscores the need of multispectral observations to better characterize the contributions of different aerosol types.

4.2.4. Comparison to CALIOP AOD

[42] We also compared forecasts to AOD retrievals from the CALIOP instrument on board the Cloud-Aerosol Lidar and Infrared Pathfinder Satellite Observations (CALIPSO) satellite [Winker *et al.*, 2009]. CALIPSO flies in a near-nadir view so that CALIOP footprints nominally fall on the satellite ground track. The CALIOP AOD product is provided

at 5 km (60 m) horizontal (vertical) resolution and was averaged to match the model horizontal resolution (27 km) and vertical grid before comparing to the model output.

[43] Figure 11 shows the results at 532 nm of CALIOP transects around 17:00 UTC 19 March (Figures 11a–11c) and 20:00 UTC 20 March (Figures 11d–11f). The AOD model output is essentially from an 11 h (14 h) forecast for the case on 19 (20) March (see section 4.2.1 about discussion of forecast range for aerosols). The model times differ from those of the CALIOP observations by ~ 40 min (~ 15 min) for the path on 19 March (20 March). Larger AOD values were produced by the DA experiment on both dates, while the patterns were similar for both experiments. As shown in Figures 11c–11f, the DA experiment agreed more with CALIOP than the NoDA experiment for both paths. The improvement through DA is particularly evident in the southeast part of the domain on 20 March. We note that CALIOP AOD measurements were retrieved only from cloud-free layers, whereas the model AOD was obtained from integration over all model layers, regardless of whether clouds were present. This difference may explain some of the discrepancies between the model-predicted and CALIOP AODs in Figure 11.

[44] The vertical distributions of 532 nm CALIOP AOD and 550 nm model AOD output corresponding to Figure 11f are given in Figure 12. Both experiments well simulated the

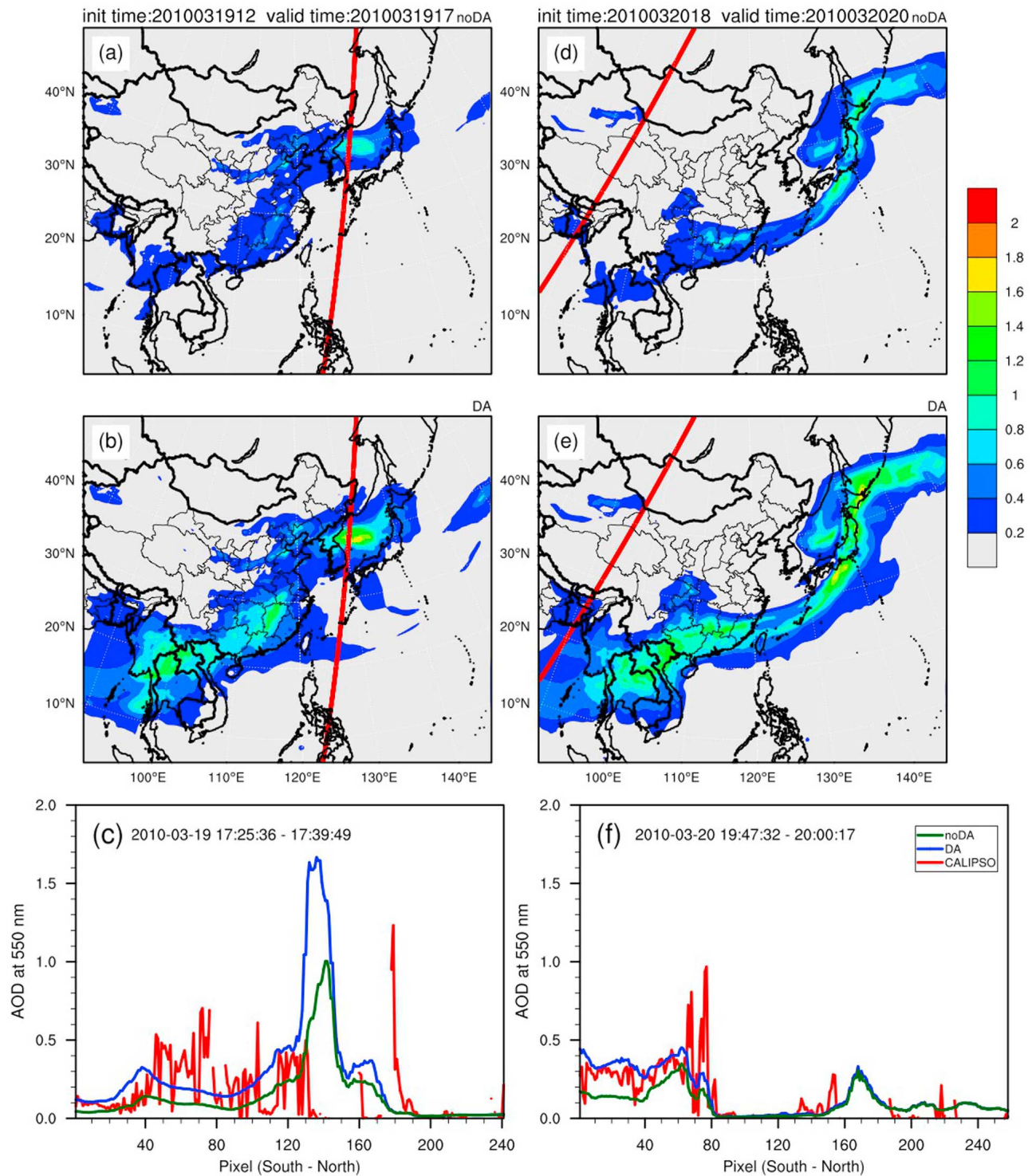


Figure 11. Model 550 nm AOD forecasts from (a, d) the NoDA experiment and (b, e) the DA experiment overlaid with CALIPSO path, and (c, f) 532 nm AOD values along the CALIPSO path from CALIOP observations (red) and 550 nm model AOD output from DA (blue) and NoDA (green) experiment. Figures 11a–11c are valid around 17:00 UTC 19 March and Figures 11d–11f around 20:00 UTC 20 March.

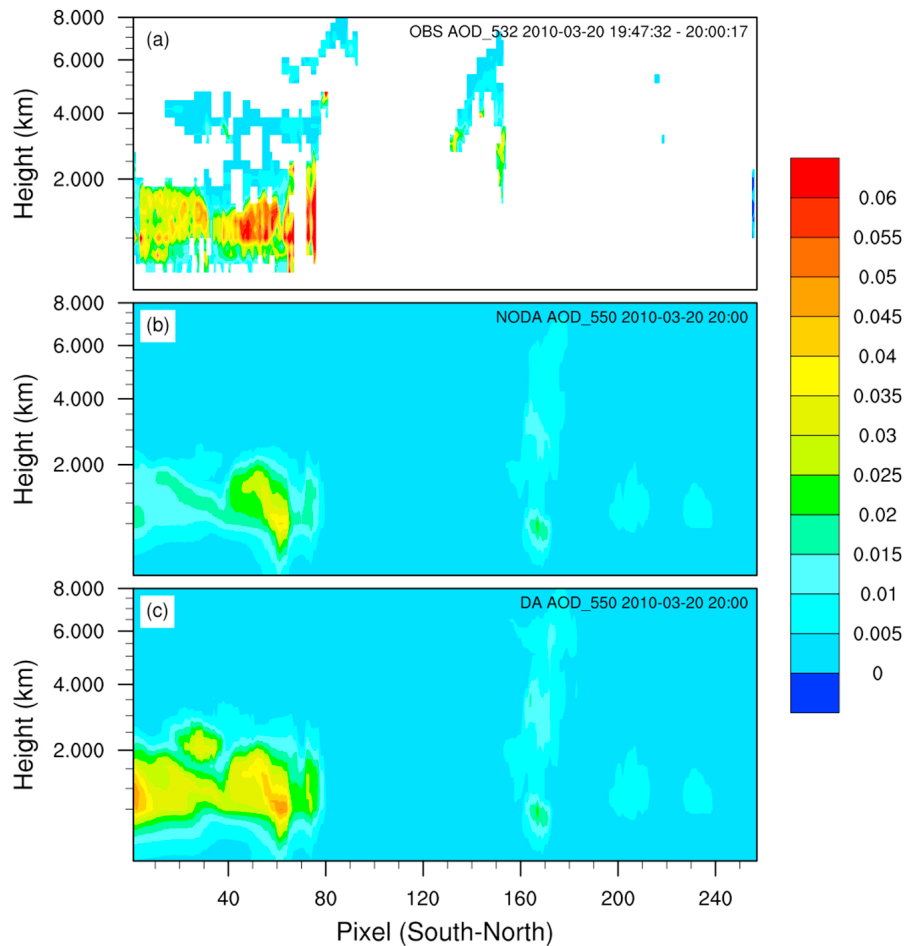


Figure 12. Similar to Figure 11f but corresponding vertical distributions of (a) 532 nm CALIOP AOD, (b) 550 nm AOD from NoDA, and (c) DA experiments around 20:00 UTC 20 March.

AOD vertical distributions within the 1 to 2 km layer in the southern part of the CALIPSO path. Clearly, the larger AOD values from the DA experiment agreed more closely with the CALIOP observations.

4.2.5. Comparison to Surface PM_{10}

[45] Model forecasts of near-surface PM_{10} were verified at 83 surface stations across China (see Figure 1 for coverage). The PM_{10} observations at all sites represented daily averages from 00:00–00:00 UTC, and 12:00 UTC was chosen as the “effective” valid time for the observations. Thus, hourly PM_{10} model output from the lowest vertical level was also averaged over 24 h periods centered at 12:00 UTC for comparison with observations.

[46] PM_{10} concentrations averaged over the 83 verification sites were uniformly greater in the experiment with AOD DA (Figure 13a), consistent with that experiment’s higher AOD values. The mean observed values reflect the passage of the dust storm, with a peak value on 21 March. The average PM_{10} values from the DA experiment were closer to the observed values except for 19 March, when PM_{10} was grossly overestimated in the DA experiment. The reason for this overestimation is unclear and subject to future investigation. However, the DA experiment’s mean value on

21 March was similar to the observed mean and corresponded to the peak intensity of the dust storm.

[47] Observed PM_{10} concentrations varied considerably across the sites (Figure 13b), especially during the dust storm period. Neither experiment consistently replicated the observed standard deviation. For example, the experiment with DA overpredicted the spread during the first several periods but underpredicted spread at later times, and other than the first two periods, the experiment without DA did not forecast spread well. While there were shortcomings of both experiments regarding spread, AOD DA produced standard deviations that were closer to the observations during the dust storm period, further suggesting DA added value to the forecasts for this extreme event.

[48] Additionally, using a 2×2 contingency table (Table 2), the equitable threat score (ETS) was calculated over the 83 sites. By selecting PM_{10} thresholds (q ; e.g., $100 \mu\text{g m}^{-3}$) to define an event, the i th site ($i = 1 \dots 83$) was placed into the proper quadrant of Table 2 based on the correspondence between the forecast (F) and observations (O) at its location. Specifically, the i th site fell into category *a* if the event was correctly predicted ($F_i \geq q$ and $O_i \geq q$); *b* if the event was forecast but did not occur ($F_i \geq q$ and $O_i < q$); *c* if an event occurred but was not forecast ($F_i < q$ and $O_i \geq q$);

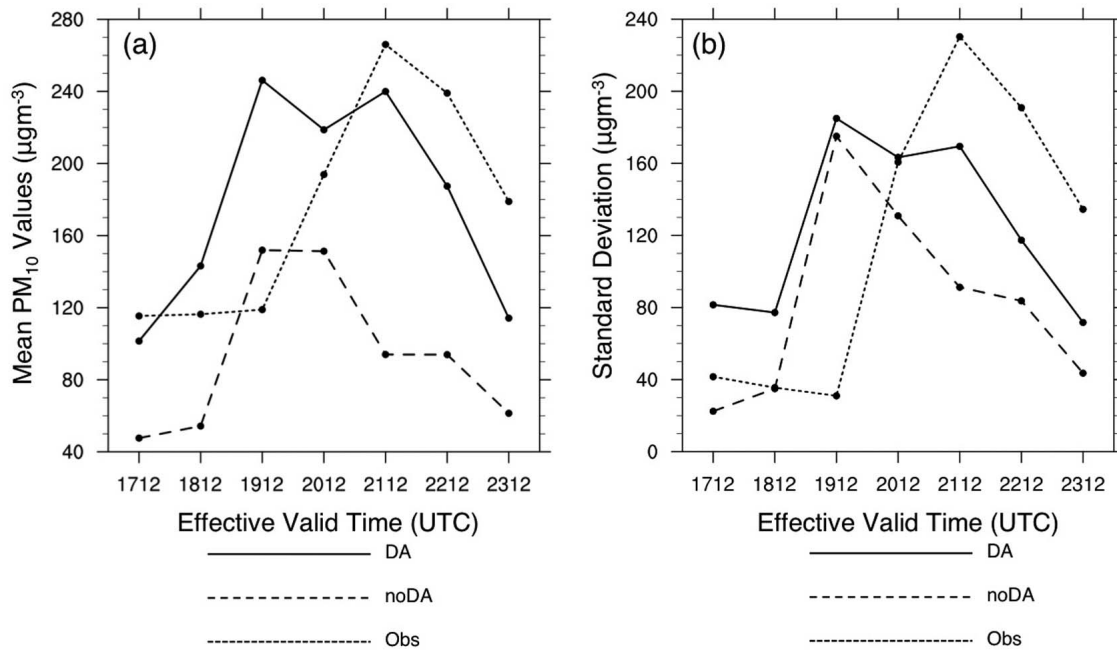


Figure 13. (a) Average PM_{10} values (μgm^{-3}) and (b) standard deviation (μgm^{-3}) over 83 stations (see Figure 1) for each “effective” valid time (section 4.2.5). The experiments with and without DA are indicated by the solid and long-dashed lines, respectively, while the observations are denoted by the short-dashed line. The x axis labels represent the day and hour (UTC) in March 2010 (i.e., 1712 means 12:00 UTC 17 March).

and d if a nonevent was correctly predicted ($F_i < q$ and $O_i < q$). Using the elements of Table 2, ETS is defined as $ETS = (a - e)/(a + b + c - e)$, where $e = (a + b)(a + c)/(a + b + c + d)$ and is the number of “hits” (elements in quadrant “a” of Table 2) due to random chance. ETS ranges from $-1/3$ to 1, with a perfect forecast achieving a score of 1 and a forecast worse than random chance scoring less than 0. Thresholds of 100 and 200 μgm^{-3} were chosen to evaluate the model forecasts since these thresholds fell within the ranges of the mean PM_{10} values (Figure 13a).

[49] For $q = 100 \mu\text{gm}^{-3}$ (Figure 14a), other than the 12:00 UTC 19 March effective valid time, assimilating AOD led to substantially higher ETSs. The improvement of the experiment with AOD DA compared to the experiment without DA was maximized around 12:00 UTC 21 March, when the dust storm was near peak intensity. In terms of ETS, the experiment with DA also produced its best forecast at that time.

[50] When the threshold was increased to $q = 200 \mu\text{gm}^{-3}$ (Figure 14b), both experiments sometimes struggled, with ETSs near or below zero for the non-dust storm periods. During these times, there were few observations that met or exceeded this higher threshold, which may have partially contributed to the low ETSs. However, during the height of the dust storm, as measured by the ETS, AOD DA resulted in improved PM_{10} forecasts.

[51] By altering the profiles of GOCART aerosol species through AOD DA, surface PM_{10} forecasts were also modified. The overall results suggest that AOD DA yields a modest improvement of surface PM_{10} forecasts, although the benefits of DA were not evident each day. Additional

improvement of PM_{10} predictions is likely to be gained by directly assimilating surface PM_{10} observations.

5. Conclusions and Future Perspectives

[52] The GSI 3DVAR DA system was expanded to assimilate MODIS AOD observations using 3-D mass concentrations of 14 GOCART aerosol species as analysis variables. The CRTM was extended to serve as the AOD observation operator (both forward operator and Jacobian) and computed model-simulated AOD from the aerosol profiles. Some developments, such as adding aerosol analysis variables in the GSI and the corresponding background error statistics, are applicable to the assimilation of any aerosol related observations. Our one-step procedure did not impose any constraints or assumptions about the relative contribution of each species’ mass concentration to the total aerosol mass concentration, in contrast to traditional two-step approaches. Thus, AOD observations could directly impact the analysis profiles of individual species. The aerosol analyses were used to initialize WRF/Chem forecasts.

Table 2. Standard 2×2 Contingency Table for Dichotomous Events

Forecast	Observed		Marginal Total
	Yes	No	
Yes	a	b	$a + b$
No	c	d	$c + d$
Marginal Total	$a + c$	$b + d$	

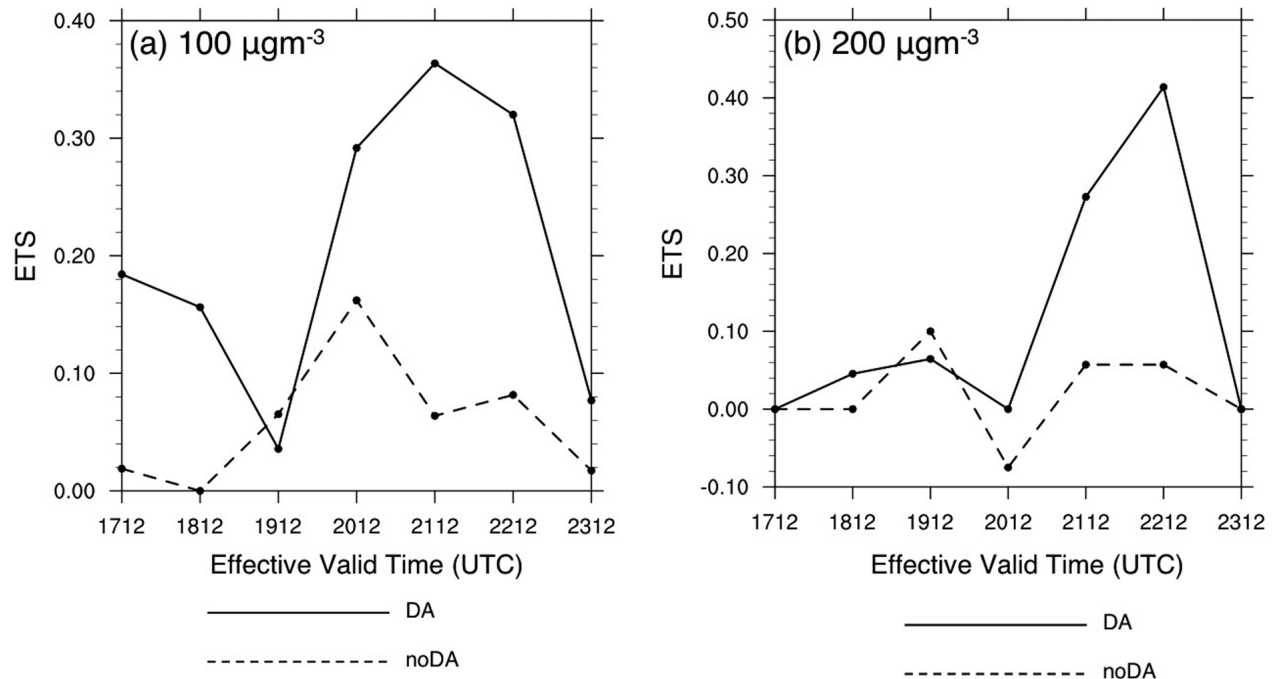


Figure 14. Equitable threat score determined over 83 stations (see Figure 1) for PM₁₀ forecasts for each “effective” valid time (section 4.2.5) using thresholds of (a) 100 and (b) 200 μgm^{-3} . The experiments with and without DA are indicated by the solid and long-dashed lines, respectively. The x axis labels represent the day and hour (UTC) in March 2010 (i.e., 1712 means 12:00 UTC 17 March).

[53] The impact of the newly developed AOD DA system was demonstrated by application to a dust storm that occurred in March 2010 over eastern Asia. Aerosol analyses and forecasts were validated against AOD observations from various sources (MODIS, AERONET, and CALIOP) and surface PM₁₀ data. The WRF/Chem model simulation without AOD DA severely underestimated the dust storm intensity, and, thus, the corresponding AOD values. However, AOD DA reduced the model low bias for aerosol forecasts by inflating the initial 3-D aerosol mass concentrations, particularly for fine mode dust species (DUST1 and DUST2). The results indicate that our one-step 3DVAR method of assimilating MODIS AOD permits concentrations of individual aerosol species to change while maintaining similar vertical structures before and after DA.

[54] Aerosol analyses and forecasts with AOD DA were substantially improved when compared to independent AOD observations from AERONET sites and CALIOP as well as surface PM₁₀ observations. The maximum dust intensity at AERONET sites were well captured by the WRF/Chem model simulation with AOD DA. Therefore, the AOD DA system developed here could be used as a tool to generate better dust storm forecasts. Moreover, we also illustrated the potential of AOD DA to improve general air quality analyses and forecasts by examining AOD from the model output and observations at the Kathmandu AERONET site, which was unaffected by the dust storm but suffers from major air pollution.

[55] The AOD DA capability we developed here is just the first step toward a more comprehensive aerosol DA system. It is fairly straightforward to expand the system to assimilate additional aerosol-related observations (e.g.,

surface measurements of particle matter, multispectral and multiangle AOD retrievals from different satellite instruments, vertical extinction profiles from ground-based and space-borne Lidar), and, thus, refine vertical structures of individual species and better quantify each species’ contribution to the total aerosol mass. New aerosol variables can be added to the state vector and the corresponding BECs determined easily. Moreover, our 3DVAR system can simultaneously assimilate MODIS AOD and meteorological observations typically used in GSI. This capability will be tested in future work to study the interaction between meteorological and aerosol assimilation.

[56] Further investigation is needed to more effectively use available aerosol-related observations. For instance, the model background can be biased for aerosols, which makes 3DVAR DA suboptimal. Therefore, developing a more advanced method considering the forecast bias [Dee, 2005] is desired and expected to extract observation information more optimally. Additionally, direct assimilation of raw radiances for aerosol analysis [Weaver *et al.*, 2007] may prove fruitful. More advanced DA techniques, such as 4DVAR and ensemble-based DA (EnDA) may be superior to 3DVAR by using orbital satellite observations at appropriate times, implicitly or explicitly using model dynamic and physical constraints, and calculating multivariate and flow-dependent forecast error correlations. However, 4DVAR and EnDA approaches are more computationally expensive and possibly impractical in cases for general chemistry assimilation with hundreds of prognostic variables. Moreover, a significant amount of work may be required to develop the tangent linear and adjoint of chemistry models in the case of 4DVAR, even

though some tools exist for automating generation of adjoint code [Sandu et al., 2003].

[57] Last, it should be recognized that DA is a supplemental tool and not the only way of improving aerosol analyses and forecasts. Chemical and aerosol models themselves should continue to be improved through more accurate estimations of emissions and better modeling of various physical and chemical processes.

[58] **Acknowledgments.** We are grateful to the Air Force Weather Agency for funding this work. Tijian Wang was partly supported by the National Key Basic Research Development Program of China (2011CB403406, 2010CB428503). AERONET Principal Investigators are also thanked for making their data available. Three anonymous reviewers provided very valuable comments and helped improve this manuscript. NCAR is sponsored by the National Science Foundation.

References

- Adhikary, B., S. Kulkarni, A. D'allura, Y. Tang, T. Chai, L. R. Leung, Y. Qian, C. E. Chung, V. Ramanathan, and G. R. Carmichael (2008), A regional scale chemical transport modeling of Asian aerosols with data assimilation of AOD observations using optimal interpolation technique, *Atmos. Environ.*, **42**(37), 8600–8615, doi:10.1016/j.atmosenv.2008.08.031.
- Amiridis, V., D. Balis, S. Kazadzis, A. Bais, E. Giannakaki, A. Papayannis, and C. Zerefos (2005), Four-year aerosol observations with a Raman lidar at Thessaloniki, Greece, in the framework of European Aerosol Research Lidar Network (EARLINET), *J. Geophys. Res.*, **110**, D21203, doi:10.1029/2005JD006190.
- Benedetti, A., and M. Fisher (2007), Background error statistics for aerosols, *Q. J. R. Meteorol. Soc.*, **133**, 391–405, doi:10.1002/qj.37.
- Benedetti, A., et al. (2009), Aerosol analysis and forecast in the European Centre for Medium-Range Weather Forecasts Integrated Forecast System: 2. Data assimilation, *J. Geophys. Res.*, **114**, D13205, doi:10.1029/2008JD011115.
- Binkowski, F. S., and S. J. Roselle (2003), Models-3 Community Multi-scale Air Quality (CMAQ) model aerosol component: 1. Model description, *J. Geophys. Res.*, **108**(D6), 4183, doi:10.1029/2001JD001409.
- Bormann, N., and J.-N. Thépaut (2004), Impact of MODIS polar winds in ECMWF's 4DVAR data assimilation system, *Mon. Weather Rev.*, **132**, 929–940, doi:10.1175/1520-0493(2004)132<0929:IOIMPWI>2.0.CO;2.
- Chin, M., R. B. Rood, S.-J. Lin, J.-F. Muller, and A. M. Thompson (2000), Atmospheric sulfur cycle simulated in the global model GOCART: Model description and global properties, *J. Geophys. Res.*, **105**, 24,671–24,687, doi:10.1029/2000JD900384.
- Chin, M., P. Ginoux, S. Kinne, O. Torres, B. N. Holben, B. N. Duncan, R. V. Martin, J. A. Logan, and A. Higurashi (2002), Tropospheric aerosol optical thickness from the GOCART model and comparisons with satellite and Sun photometer measurements, *J. Atmos. Sci.*, **59**, 461–483, doi:10.1175/1520-0469(2002)059<0461:TAOTFT>2.0.CO;2.
- Collins, W. D., P. J. Rasch, B. E. Eaton, B. V. Khattatov, and J.-F. Lamarque (2001), Simulating aerosols using a chemical transport model with assimilation of satellite aerosol retrievals: Methodology for INDOEX, *J. Geophys. Res.*, **106**, 7313–7336, doi:10.1029/2000JD900507.
- Courtier, P., J.-N. Thépaut, and A. Hollingsworth (1994), A strategy for operational implementation of 4D-Var, using an incremental approach, *Q. J. R. Meteorol. Soc.*, **120**, 1367–1387, doi:10.1002/qj.49712051912.
- d'Almeida, G. A., P. Koepke, and E. P. Shettle (1991), *Atmospheric Aerosols: Global Climatology and Radiative Characteristics*, 561 pp., A. Deepak, Hampton, Va.
- Dee, D. P. (2005), Bias and data assimilation, *Q. J. R. Meteorol. Soc.*, **131**, 3323–3343, doi:10.1256/qj.05.137.
- Derber, J., and A. Rosati (1989), A global oceanic data assimilation system, *J. Phys. Oceanogr.*, **19**, 1333–1347, doi:10.1175/1520-0485(1989)019<1333:AGODAS>2.0.CO;2.
- Derber, J. C., and W.-S. Wu (1998), The use of TOVS cloud-cleared radiances in the NCEP SSI analysis system, *Mon. Weather Rev.*, **126**, 2287–2299, doi:10.1175/1520-0493(1998)126<2287:TUOTCC>2.0.CO;2.
- Forster, P., et al. (2007), Changes in atmospheric constituents and in radiative forcing, in *Climate Change 2007: The Physical Science Basis. Contribution of Working Group I to the Fourth Assessment Report of the Intergovernmental Panel on Climate Change*, edited by S. Solomon et al., chap. 2, pp. 129–234, Cambridge Univ. Press, Cambridge, U. K.
- Gauthier, P., M. Tanguay, S. Laroche, S. Pellerin, and J. Morneau (2007), Extension of 3DVAR to 4DVAR: Implementation of 4DVAR at the Meteorological Service of Canada, *Mon. Weather Rev.*, **135**, 2339–2354, doi:10.1175/MWR3394.1.
- Generoso, S., F.-M. Bréon, F. Chevallier, Y. Balkanski, M. Schulz, and I. Bey (2007), Assimilation of POLDER aerosol optical thickness into the LMDz-INCA model: Implications for the Arctic aerosol burden, *J. Geophys. Res.*, **112**, D02311, doi:10.1029/2005JD006954.
- Gilbert, J. C., and C. Lemaréchal (1989), Some numerical experiments with variable-storage quasi-Newton algorithms, *Math. Program.*, **45**, 407–435, doi:10.1007/BF01589113.
- Ginoux, P., M. Chin, I. Tegen, J. Prospero, B. Holben, O. Dubovik, and S.-J. Lin (2001), Sources and distributions of dust aerosols simulated with the GOCART model, *J. Geophys. Res.*, **106**, 20,225–20,273, doi:10.1029/2000JD000053.
- Grell, G. A., S. E. Peckham, R. Schmitz, S. A. McKeen, G. Frost, W. C. Skamarock, and B. Eder (2005), Fully coupled “online” chemistry within the WRF model, *Atmos. Environ.*, **39**, 6957–6975, doi:10.1016/j.atmosenv.2005.04.027.
- Guenther, A., P. Zimmerman, and M. Wildermuth (1994), Natural volatile organic compound emission rate estimates for U.S. woodland landscapes, *Atmos. Environ.*, **28**, 1197–1210, doi:10.1016/1352-2310(94)90297-6.
- Hale, G. M., and M. R. Querry (1973), Optical constants of water in the 200-nm to 200- μ m wavelength region, *Appl. Opt.*, **12**, 555–563, doi:10.1364/AO.12.000555.
- Han, Y., P. van Delst, Q. Liu, F. Weng, B. Yan, R. Treadon, and J. Derber (2006), JCSDA Community Radiative Transfer Model (CRTM)—Version 1, *NOAA Tech. Rep. NESDIS 122*, 33 pp., NOAA, Silver Spring, Md.
- Hess, M., P. Koepke, and I. Schult (1998), Optical properties of aerosols and clouds: The software package OPAC, *Bull. Am. Meteorol. Soc.*, **79**, 831–844, doi:10.1175/1520-0477(1998)079<0831:OPOAAC>2.0.CO;2.
- Holben, B. N., et al. (1998), AERONET—A federated instrument network and data archive for aerosol characterization, *Remote Sens. Remote Sens. Environ.*, **66**, 1–16, doi:10.1016/S0034-4257(98)00031-5.
- Hsu, N. C., S.-C. Tsay, M. D. King, and J. R. Herman (2004), Aerosol properties over bright-reflecting source regions, *IEEE Trans. Geosci. Remote Sens.*, **42**, 557–569, doi:10.1109/TGRS.2004.824067.
- Hsu, N. C., S.-C. Tsay, M. D. King, and J. R. Herman (2006), Deep Blue retrieval of Asia aerosol properties during ACE-Asia, *IEEE Trans. Geosci. Remote Sens.*, **44**, 3180–3195, doi:10.1109/TGRS.2006.879540.
- Ide, K., P. Courtier, M. Ghil, and A. Lorenc (1997), Unified notation for data assimilation: Operational, sequential and variational, *J. Meteorol. Soc. Jpn.*, **75**, 181–189.
- Ignatov, A., J. Sapper, I. Laszlo, N. Nalli, and K. Kidwell (2004), Operational aerosol observations (AEROBS) from AVHRR/3 on board NOAA-KLM satellites, *J. Atmos. Oceanic Technol.*, **21**, 3–26, doi:10.1175/1520-0426(2004)021<0003:OAOAFO>2.0.CO;2.
- Kahn, R. A., B. J. Gaitley, M. J. Garay, D. J. Diner, T. Eck, A. Smirnov, and B. N. Holben (2010), Multiangle Imaging Spectroradiometer global aerosol product assessment by comparison with the Aerosol Robotic Network, *J. Geophys. Res.*, **115**, D23209, doi:10.1029/2010JD014601.
- Kahnert, M. (2008), Variational data analysis of aerosol species in a regional CTM: Background error covariance constraint and aerosol optical observation operators, *Tellus, Ser. B*, **60**, 753–770, doi:10.1111/j.1600-0889.2008.00377.
- Kaufman, Y. J., D. Tanré, and O. Boucher (2002), A satellite view of aerosols in the climate system, *Nature*, **419**, 215–223, doi:10.1038/nature01091.
- King, M. D., J. Yoram, J. Kaufman, D. Tanré, and T. Nakajima (1999), Remote sensing of tropospheric aerosols from space: Past, present and future, *Bull. Am. Meteorol. Soc.*, **80**, 2229–2259, doi:10.1175/1520-0477(1999)080<2229:RSOTAF>2.0.CO;2.
- Kleist, D. T., D. F. Parrish, J. C. Derber, R. Treadon, W.-S. Wu, and S. Lord (2009), Introduction of the GSI into the NCEP Global Data Assimilation System, *Weather Forecast.*, **24**, 1691–1705, doi:10.1175/2009WAF2222201.1.
- Lamarque, J.-F., J. T. Kiehl, P. G. Hess, W. D. Collins, L. K. Emmons, P. Ginoux, C. Luo, and X. X. Tie (2005), Response of a coupled chemistry-climate model to changes in aerosol emissions: Global impact on the hydrological cycle and the tropospheric burdens of OH, ozone, and NO_x, *Geophys. Res. Lett.*, **32**, L16809, doi:10.1029/2005GL023419.
- Liu, Q., and F. Weng (2006), Advanced doubling-adding method for radiative transfer in planetary atmosphere, *J. Atmos. Sci.*, **63**(12), 3459–3465, doi:10.1175/JAS3808.1.
- Lorenc, A. C. (1981), A global three-dimensional multivariate statistical interpolation scheme, *Mon. Weather Rev.*, **109**, 701–721, doi:10.1175/1520-0493(1981)109<0701:AGTDM>2.0.CO;2.
- Lorenc, A. C. (1986), Analysis method for numerical weather prediction, *Q. J. R. Meteorol. Soc.*, **112**, 1177–1194, doi:10.1002/qj.49711247414.

- Lorenc, A. C., et al. (2000), The Met. Office global three-dimensional variational data assimilation scheme, *Q. J. R. Meteorol. Soc.*, *126*, 2991–3012, doi:10.1002/qj.49712657002.
- Mangold, A., et al. (2011), Aerosol analysis and forecast in the European Centre for Medium-Range Weather Forecasts Integrated Forecast System: 3. Evaluation by means of case studies, *J. Geophys. Res.*, *116*, D03302, doi:10.1029/2010JD014864.
- McNally, A. P., J. C. Derber, W. Wu, and B. B. Katz (2000), The use of TOVS level-1b radiances in the NCEP SSI analysis system, *Q. J. R. Meteorol. Soc.*, *126*, 689–724, doi:10.1002/qj.49712656315.
- Morcrette, J.-J., et al. (2009), Aerosol analysis and forecast in the European Centre for Medium-Range Weather Forecasts Integrated Forecast System: Forward modeling, *J. Geophys. Res.*, *114*, D06206, doi:10.1029/2008JD011235.
- Navon, I. M., and D. M. Legler (1987), Conjugate-gradient methods for large-scale minimization in meteorology, *Mon. Weather Rev.*, *115*(8), 1479–1502, doi:10.1175/1520-0493(1987)115<1479:CGMFLS>2.0.CO;2.
- Niu, T., S. L. Gong, G. F. Zhu, H. L. Liu, X. Q. Hu, C. H. Zhou, and Y. Q. Wang (2008), Data assimilation of dust aerosol observations for the CUACE/dust forecasting system, *Atmos. Chem. Phys.*, *8*, 3473–3482, doi:10.5194/acp-8-3473-2008.
- Parrish, D. F., and J. C. Derber (1992), The National Meteorological Center's spectral statistical interpolation analysis system, *Mon. Weather Rev.*, *120*, 1747–1763, doi:10.1175/1520-0493(1992)120<1747:TNMCSS>2.0.CO;2.
- Pope, C. A., R. T. Burnett, M. J. Thun, E. E. Calle, D. Krewski, K. Ito, and G. D. Thurston (2002), Lung cancer, cardiopulmonary mortality, and long-term exposure to fine particulate air pollution, *J. Am. Med. Assoc.*, *287*(9), 1132–1141, doi:10.1001/jama.287.9.1132.
- Rabier, F., A. McNally, E. Andersson, P. Courtier, P. Undén, J. Eyre, A. Hollingsworth, and F. Bouttier (1998), The ECMWF implementation of three-dimensional variational assimilation (3D-Var). II: Structure functions, *Q. J. R. Meteorol. Soc.*, *124*, 1809–1829, doi:10.1002/qj.49712455003.
- Rabier, F., H. Jarvinen, E. Klinker, J.-F. Mahfouf, and A. Simmons (2000), The ECMWF operational implementation of four-dimensional variational assimilation I: Experimental results with simplified physics, *Q. J. R. Meteorol. Soc.*, *126*, 1143–1170, doi:10.1256/smsqj.56414.
- Remer, L. A., et al. (2005), The MODIS aerosol algorithm, products, and validation, *J. Atmos. Sci.*, *62*, 947–973, doi:10.1175/JAS3385.1.
- Rodwell, M. (2005), The local and global impact of the recent change in aerosol climatology, *ECMWF Newsl.*, *105*, 17–23.
- Sandu, A., D. Daescu, and G. R. Carmichael (2003), Direct and adjoint sensitivity analysis of chemical kinetic systems with KPP: Part I—Theory and software tools, *Atmos. Environ.*, *37*, 5083–5096, doi:10.1016/j.atmosenv.2003.08.019.
- Schubert, S. D., R. B. Rood, and J. Pfendtner (1993), An assimilated dataset for Earth science applications, *Bull. Am. Meteorol. Soc.*, *74*, 2331–2342, doi:10.1175/1520-0477(1993)074<2331:AADFES>2.0.CO;2.
- Schutgens, N. A. J., T. Miyoshi, T. Takemura, and T. Nakajima (2010), Applying an ensemble Kalman filter to the assimilation of AERONET observations in a global aerosol transport model, *Atmos. Chem. Phys.*, *10*, 2561–2576, doi:10.5194/acp-10-2561-2010.
- Sekiyama, T. T., T. Y. Tanaka, A. Shimizu, and T. Miyoshi (2010), Data assimilation of CALIPSO aerosol observations, *Atmos. Chem. Phys.*, *10*, 39–49, doi:10.5194/acp-10-39-2010.
- Sekiyama, T. T., T. Y. Tanaka, T. Maki, and M. Mikami (2011), The effects of snow cover and soil moisture on Asian dust: II. Emission estimation by Lidar data assimilation, *SOLA*, *7A*, 40–43, doi:10.2151/sola.7A-011.
- Sharma, C. K. (1997), Urban air quality of Kathmandu Valley “Kingdom of Nepal,” *Atmos. Environ.*, *31*, 2877–2883, doi:10.1016/S1352-2310(96)00346-9.
- Simpson, D., A. Guenther, C. N. Hewitt, and R. Steinbrecher (1995), Biogenic emissions in Europe I. Estimates and uncertainties, *J. Geophys. Res.*, *100*, 22,875–22,890, doi:10.1029/95JD02368.
- Skamarock, W. C., J. B. Klemp, J. Dudhia, D. O. Gill, D. M. Barker, M. G. Duda, X.-Y. Huang, W. Wang, and J. G. Powers (2008), A description of the Advanced Research WRF version 3, *NCAR Tech. Note NCAR/TN-475+STR*, 113 pp., Natl. Cent. for Atmos. Res., Boulder, Colo.
- Stockwell, W. R., F. Kirchner, M. Kuhn, and S. Seefeld (1997), A new mechanism for regional atmospheric chemistry modeling, *J. Geophys. Res.*, *102*(D22), 25,847–25,879, doi:10.1029/97JD00849.
- Streets, D. G., et al. (2003), An inventory of gaseous and primary aerosol emissions in Asia in the year 2000, *J. Geophys. Res.*, *108*(D21), 8809, doi:10.1029/2002JD003093.
- Torres, O., P. K. Bhartia, J. R. Herman, A. Sinyuk, and B. Holben (2002), A long-term record of aerosol optical thickness from TOMS observations and comparison to AERONET measurements, *J. Atmos. Sci.*, *59*, 398–413, doi:10.1175/1520-0469(2002)059<0398:ALTROA>2.0.CO;2.
- Torres, O., A. Tanskanen, B. Veihelmann, C. Ahn, R. Braak, P. K. Bhartia, P. Veeckind, and P. Levelt (2007), Aerosols and surface UV products from Ozone Monitoring Instrument observations: An overview, *J. Geophys. Res.*, *112*, D24S47, doi:10.1029/2007JD008809.
- van de Hulst, H. C. (1957), *Light Scattering by Small Particles*, 470 pp., John Wiley, New York.
- Wang, X., D. M. Barker, C. Snyder, and T. M. Hamill (2008), A hybrid ETKF-3DVAR data assimilation scheme for the WRF model. Part I: Observing system simulation experiment, *Mon. Weather Rev.*, *136*, 5116–5131, doi:10.1175/2008MWR2444.1.
- Weaver, C., A. da Silva, M. Chin, P. Ginoux, O. Dubovik, D. Flittner, A. Zia, L. Remer, B. Holben, and W. Gregg (2007), Direct insertion of MODIS radiances in a global aerosol transport model, *J. Atmos. Sci.*, *64*, 808–827, doi:10.1175/JAS3838.1.
- Welton, E. J., and J. R. Campbell (2002), Micropulse lidar signals: Uncertainty analysis, *J. Atmos. Oceanic Technol.*, *19*, 2089–2094, doi:10.1175/1520-0426(2002)019<2089:MLSUA>2.0.CO;2.
- Wesely, M. L. (1989), Parameterization of surface resistance to gaseous dry deposition in regional-scale numerical models, *Atmos. Environ.*, *23*, 1293–1304, doi:10.1016/0004-6981(89)90153-4.
- Winker, D. M., M. A. Vaughan, A. Omar, Y. Hu, K. A. Powell, Z. Liu, W. H. Hunt, and S. A. Young (2009), Overview of the CALIPSO mission and CALIOP data processing algorithms, *J. Atmos. Oceanic Technol.*, *26*, 2310–2323, doi:10.1175/2009JTECHA1281.1.
- Wu, W.-S., D. F. Parrish, and R. J. Purser (2002), Three-dimensional variational analysis with spatially inhomogeneous covariances, *Mon. Weather Rev.*, *130*, 2905–2916, doi:10.1175/1520-0493(2002)130<2905:TDVAWS>2.0.CO;2.
- Yu, H., R. E. Dickinson, M. Chin, Y. J. Kaufman, B. Geogdzhayev, and M. I. Mishchenko (2003), Annual cycle of global distributions of aerosol optical depth from integration of MODIS retrievals and GOCART model simulations, *J. Geophys. Res.*, *108*(D3), 4128, doi:10.1029/2002JD002717.
- Yumimoto, K., I. Uno, N. Sugimoto, A. Shimizu, and S. Satake (2007), Adjoint inverse modeling of dust emission and transport over East Asia, *Geophys. Res. Lett.*, *34*, L08806, doi:10.1029/2006GL028551.
- Yumimoto, K., I. Uno, N. Sugimoto, A. Shimizu, Z. Liu, and D. M. Winker (2008), Adjoint inversion modeling of Asian dust emission using lidar observations, *Atmos. Chem. Phys.*, *8*(11), 2869–2884, doi:10.5194/acp-8-2869-2008.
- Zhang, J., and J. S. Reid (2006), MODIS aerosol product analysis for data assimilation: Assessment of level 2 aerosol optical thickness retrievals, *J. Geophys. Res.*, *111*, D22207, doi:10.1029/2005JD006898.
- Zhang, J., J. S. Reid, D. Westphal, N. Baker, and E. Hyer (2008), A system for operational aerosol optical depth data assimilation over global oceans, *J. Geophys. Res.*, *113*, D10208, doi:10.1029/2007JD009065.
- Zhang, Q., et al. (2009), Asian emissions in 2006 for the NASA INTEX-B mission, *Atmos. Chem. Phys.*, *9*, 5131–5153, doi:10.5194/acp-9-5131-2009.

Y.-H. Lee, H.-C. Lin, Z. Liu, and C. S. Schwartz, National Center for Atmospheric Research, PO Box 3000, Boulder, CO 80303-3000, USA. (liuz@ucar.edu)

Q. Liu, Joint Center for Satellite Data Assimilation, 5200 Auth Rd., Rm. 703, Camp Springs, MD 20746, USA.

T. Wang, School of Atmospheric Science, Nanjing University, Hankou Rd. 22, Nanjing 210093, China.